Temporal Entanglement from Holographic Entanglement Entropy

Michal P. Heller, ^{1,2,*} Fabio Ori, ^{1,†} and Alexandre Serantes, ¹Department of Physics and Astronomy, Ghent University, 9000 Ghent, Belgium, ²Institute of Theoretical Physics and Mark Kac Center for Complex Systems Research, Jagiellonian University, 30-348 Cracow, Poland

(Received 22 August 2025; accepted 30 September 2025; published 6 November 2025)

Recently, several notions of entanglement in time have emerged as a novel frontier in quantum many-body physics, quantum field theory, and gravity. We propose a systematic prescription to characterize temporal entanglement in relativistic quantum field theory in a general state for an arbitrary subregion on a flat, constant time slice in a flat spacetime. Our prescription starts with the standard entanglement entropy of a spatial subregion and amounts to transporting the unchanged subregion to boosted time slices all the way across the light cone when it becomes, in general, a complex characterization of the corresponding temporal subregion. For holographic quantum field theories, our prescription amounts to an analytic continuation of all codimension-two bulk extremal surfaces satisfying the homology constraint and picking the one with the smallest real value of the area as the leading saddle point. We implement this prescription for holographic conformal field theories in thermal states on both a two-dimensional Lorentzian cylinder and three-dimensional Minkowski space, and we show that it leads to results with self-consistent physical properties of temporal entanglement.

DOI: 10.1103/qlsv-gp22 Subject Areas: Gravitation, Particles and Fields, String Theory

I. INTRODUCTION

Entanglement and its entropy have been among the very few key notions shaping the development of theoretical physics in the last two decades. Impressive progress includes the establishment of entanglement-inferred tensor network algorithms for ab initio simulation of quantum many-body systems on classical computers [1,2], the characterization of topological orders [3], shedding light on thermalization of closed quantum systems [4,5], a new understanding of irreversibility of renormalization group flows in quantum field theory [6], and the geometrization of quantum field theory entanglement within the holographic duality [7–9] as well as studying its implications for the black hole information paradox [10]. All these paradigmshifting developments stem from the standard notion of entanglement entropy associated with a bipartition of quantum systems into spatial subregions on a constant

*Contact author: michal.p.heller@ugent.be
†Contact author: fabio.ori@ugent.be

*Contact author: alexandre.serantesrubianes@ugent.be

Published by the American Physical Society under the terms of the Creative Commons Attribution 4.0 International license. Further distribution of this work must maintain attribution to the author(s) and the published article's title, journal citation, and DOI. time slice or appropriate algebraic quantum field theory formalizations of this notion.

While this entanglement in space is arguably quite well understood by now, the notion of entanglement in time is not. In the first place, such a notion is not apparent from the basics of quantum mechanics. Instead, it originates from the field of tensor networks and attempts within it to lower the complexity of algorithms modeling unitary time evolution by devising clever contraction schemes leading to the emergence of the paradigmatic matrix product state tensor networks along the temporal rather than spatial direction [11,12]. Such a structure allows one to define temporal reduced density matrices of several kinds and obtain their characterization in terms of Renyi entropies [11–15], or their pseudoentropy generalizations to non-Hermitian matrices [16].

In the context of relativistic quantum field theories, as originally proposed in Refs. [17,18] (see also Ref. [19]), closed-form expressions for single interval entanglement entropy of conformal field theory (CFT) in two spacetime dimensions allow for an explicit analytic continuation to a temporal domain, leading to a notion of timelike entanglement entropy. For example, in the vacuum state in Minkowski space for a single interval of length Δx , the entanglement entropy reads

$$S = \frac{c}{3} \log \frac{\Delta x}{\delta},\tag{1}$$

where c is the central charge and δ is a short-distance cutoff [20,21]. The analytic continuation in question amounts to the replacement $\Delta x \rightarrow i\Delta t$, yielding a quantity of the same logarithmic dependence but now on Δt and having a constant imaginary offset

$$S = \frac{c}{3} \log \frac{\Delta t}{\delta} + i \frac{\pi}{6} c, \tag{2}$$

where the principal branch of the logarithm function is picked. Recently, it was shown in one particular example that a similar analytic continuation agrees with the generalization of the von Neumann entropy computed using temporal matrix product states, connecting the two hitherto independent lines of research on temporal entanglement [22]. In Refs. [17,18], the quantity encapsulated by Eq. (2) was referred to as timelike entanglement entropy (and for strongly coupled quantum field theories with a large number of microscopic constituents, it was referred to as holographic timelike entanglement entropy).

While our ability to explicitly compute entanglement entropy in a generic quantum field theory is very limited and closed-form expressions like Eq. (1) are extremely scarce, for strongly coupled quantum field theories with a large number of microscopic constituents, the entanglement entropy has proven surprisingly simple to obtain. In this case, the entanglement entropy is given in terms of the area A of the extremal surface attached to the spatial subregion of interest lying on the asymptotic boundary of the higher-dimensional geometry where holographic quantum field theories are defined (see Refs. [23,24] for the original proposals, Refs. [25–27] for approaches to a derivation, and Refs. [7–9] for reviews). More precisely, it is given by the associated Bekenstein-Hawking entropy

$$S = \frac{A}{4G_N},\tag{3}$$

where G_N is the gravitational constant in holography. Given the simplicity of how holography geometrizes entanglement entropy and the aforementioned scarcity of exact expressions for entanglement entropy in other quantum field theories, it is natural to expect that key progress on our understanding of temporal entanglement in quantum field theory will occur through AdS/CFT.

Since temporal entanglement in quantum field theory can be defined by an analytic continuation, it should come as no surprise that, holographically, the relevant geometric notion will be an analytic continuation of the extremal surfaces geometrizing entanglement entropy, such that they are anchored on a timelike subregion. In Ref. [28], we identified that such extremal surfaces will be complex, in general; i.e., they perceive the bulk geometry for complex rather than real spacetime coordinates. This finding connects with earlier holographic studies of complex geodesics, which are one-dimensional extremal surfaces, in the

context of approximating boundary correlation functions [29–31]. The key difference from the holographic dual proposed earlier by Refs. [17,18] is that the complex extremal surface is a fully covariant object and not a piecewise surface obtained by a union of real extremal surfaces with different signatures (see Ref. [28] for a detailed comparison between the two).

The key open problem that we address in the present article originates from the existence of multiple complex extremal surfaces satisfying the same boundary condition. This problem appears, for example, in the paradigmatic example of black hole spacetimes corresponding to thermal or thermofield double states in dual quantum field theory in three and more spacetime dimensions [28]. In the present paper, we identify another important instance where there are multiple complex extremal surface candidates to define holographic timelike entanglement entropy.

In the context of entanglement entropy, it is clear how to proceed when there are multiple extremal surfaces [32,33]: All real extremal surfaces homologous to the subregion give saddle-point contributions to the holographic entanglement entropy, and the one with the smallest area is the dominant one. The remaining saddles give subleading contributions to the holographic entanglement entropy, exponentially suppressed in the difference of areas with respect to the leading saddle. The presence of multiple saddles in the holographic entanglement entropy is responsible, for example, for entanglement entropy being consistent with the cluster decomposition principle of quantum field theory.

What we propose in the present work is a prescription for computing holographic timelike entanglement entropy even if there are multiple nontrivial complex extremal surface candidates. Our guiding principle is that the quantity we define holographically respects the UV-IR correspondence [34]. In particular, the key self-consistency condition for us will be that, for sufficiently small temporal subregions in general excited states, this quantity reduces to the vacuum state answer.

We define timelike entanglement entropy in terms of entanglement entropy by "rotating" the entangling region from spacelike to timelike, going around the light cone as illustrated in Fig. 1, which, in particular, transforms Eq. (1) to Eq. (2). We propose the following steps:

- Identify the complex extremal surfaces that can be obtained via such analytic continuation past the light cone of the real extremal surfaces relevant for (spacelike) holographic entanglement entropy.
- (2) Among these configurations, choose the one that minimizes the real part of the area.

As we show, because of the properties of entanglement entropy for spatial subregions in the vicinity of the light cone, in holography, this analytic continuation respects the UV-IR correspondence and reproduces the vacuum answer for small subsystems in an excited state. As a result, in

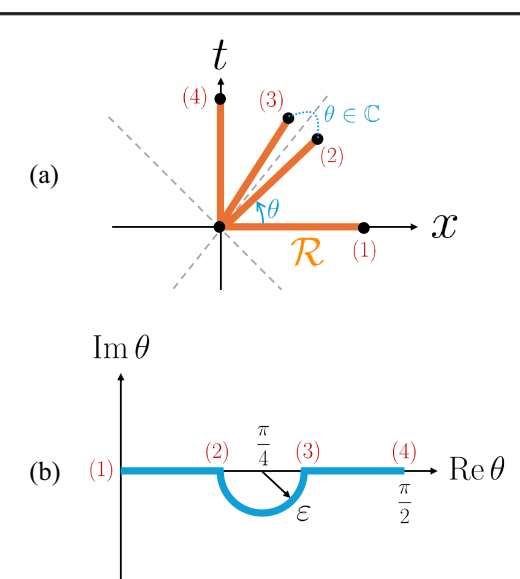


FIG. 1. (a) Geometrical analytic continuation of the boundary region \mathcal{R} . Starting from a region that lies on a constant time slice (1), the light cone is crossed by slightly complexifying the angle θ when still in the spacelike regime (2). Once the timelike regime is reached (3), the angle can be increased further to attain purely temporal separations (4). (b) Trajectory followed by the angle θ in the analytic continuation. The light cone is crossed by evading the divergence associated with the proper size of the subregion going to 0 when $\theta = \pi/4$ with a circle of arbitrarily small radius ε in the complex θ plane.

holography, our prescription for timelike entanglement entropy is a natural generalization and a direct consequence of the prescription for holographic entanglement entropy.

II. KEY IDEA

A. General quantum field theory

We consider quantum field theories primarily in *d*-dimensional Minkowski spacetime. Later in the paper, we also consider theories on a two-dimensional Lorentzian cylinder, where the spatial direction is a circle.

We seek a purely Lorentzian approach to defining timelike entanglement entropy. Extrapolating from Eqs. (1) and (2) and the results of Refs. [17,18], we propose to *define* timelike entanglement entropy by the analytic continuation of standard entanglement entropy as the spacelike subregion is morphed into a timelike one.

We want to keep the embedding of the spacelike subregion on the constant time slice fixed and "rotate" this constant time slice in the longitudinal plane spanned by the time t and a chosen spatial direction x; see Fig. 1(a). The rotation is specified by an angle θ running between 0 (the original spatial subregion) and $\pi/2$. Past the light cone located at $\theta = \pi/4$, this approach produces subregions extending along a timelike direction, as desired.

As in the case of Lorentzian correlation functions obtained from Euclidean correlators, the subtlety lies on

the codimension-one hypersurface where the subregion becomes null. There, the proper size of the subregion goes to zero, and a UV regularization is required. We avoid this singularity in the entanglement entropy by an infinitesimally small detour into complexified Minkowski space. We achieve this by complexifying the rotation angle around $\theta = \pi/4$ [see Fig. 1(b)]. Coming back to Lorentzian correlators, our prescription can be thought of as a natural generalization of real-time n-point functions to extended objects: While here we pursue its application to entanglement entropy, the same method could also be employed with, for example, Wilson loops.

The procedure outlined above can be applied to any analytic expression for entanglement entropy, such as Eq. (1), and produce a timelike generalization, such as Eq. (2). However, given the aforementioned scarcity of such exact results, the true power of our approach lies in allowing one to explicitly compute timelike entanglement entropy in holographic setups, which is the focal point of the present article.

B. Holography

In holography, when there exists only a single extremal surface satisfying a given asymptotic boundary condition in the spacelike regime—which is, by default, the single contribution to holographic entanglement entropy—the rotation outlined in Fig. 1 transforms it into a unique complex extremal surface anchored on a now timelike subregion. For example, this is the situation in holographic conformal field theories in their vacuum state considered in Ref. [28]. In this case, the idea of the continuous spacetime transformation of a subregion that we introduced above does not add much new information.

The situation changes significantly when multiple extremal surfaces satisfy the homology constraint. As we have previously noted, each of these surfaces should be regarded as a saddle point, and saddle points are known to exchange dominance depending on the parameters that define them. This idea is well known in the holographic literature and features prominently, for example, in holographic studies of the mutual information [32]. In the case at hand, the varying parameter specifying the saddles (extremal surfaces) is the angle θ (see Fig. 1). The saddles clearly also depend on the shape of the subregion, but we keep it fixed.

As a result, the holographic implementation of the spacetime transformation of Fig. 1 in the spacelike regime, i.e., for $\theta \leq \pi/4 - \varepsilon$, requires us to keep track of all the extremal surfaces obeying the homology constraint as a function of θ . In particular, for a fixed subregion shape, this number can change as a function of θ . Subsequently, all these contributions to the holographic entanglement entropy, the leading and subleading saddles existing at $\theta = \pi/4 - \varepsilon$ with $0 < \varepsilon \ll 1$, are analytically continued past the light cone to the timelike regime, i.e., $\theta \geq \pi/4 + \varepsilon$.

In the timelike regime, the dominant contribution to the holographic timelike entanglement entropy comes, as usual, from the saddle that has the smallest real value of the area. Crucially, this result does not necessarily imply that this contribution dominates the holographic entanglement entropy because taking the leading saddle in the spacelike regime associated with the limit $G_N \to 0$ does not necessarily commute with the analytic continuation.

In subsequent sections, we will explicitly apply this prescription to the four-dimensional black hole dual to a thermal state in a three-dimensional holographic conformal field theory in Minkowski space (see Sec. III) and to the three-dimensional black hole dual to a thermal state in a two-dimensional conformal field theory on a Lorentzian cylinder (see Sec. IV).

C. Comments

It is important to emphasize that the prescription outlined above is valid for *any* state in flat spacetimes and for any flat subregion.

Furthermore, the light-cone regulator ε should be understood in the limiting sense, i.e., $\varepsilon \to 0^+$. Since ultimately in generic cases holographic entanglement entropy is calculated numerically, in practice, the limit is probed by taking progressively smaller but nonzero ε and seeing indications of numerical convergence.

In contrast to the holographic entanglement entropy, which one can compute by considering the portion of the bulk limited by future- and past-pointing light rays emanating from the subregion, our definition of holographic timelike entanglement entropy necessarily requires the understanding of all saddle-point contributions to the holographic entanglement entropy right before the light cone is crossed as the parameter θ is varied and then transforming them to satisfy the desired boundary condition given by the timelike subregion. As a result, holographic timelike entanglement entropy as we define it, at least at this superficial level, requires more information about the bulk than the holographic entanglement entropy.

Moreover, it is easy to understand how the UV-IR correspondence emerges from our prescription. Note that the transformation outlined in Fig. 1 keeps the shape of the subregion intact. As the light cone is approached from the spacelike domain where the quantity one computes is holographic entanglement entropy, the proper size of the subregion along one of the directions goes to zero as a result of the Lorentz contraction. This process makes the subregion a very thin slab for which one expects the extremal surface that gives the dominant contribution to the holographic entanglement entropy to lie very close to the asymptotic boundary. Subsequently, this universal contribution that is sensitive to the vacuum physics is analytically continued to the timelike regime.

In addition, let us emphasize that keeping the shape of the subregion rigid during the rotations, which we view as a natural condition to impose, eliminates most of the potential ambiguities in the analytic continuation of the entanglement entropy. The only ambiguity remaining is related to going "below" or "above" the light cone (see Fig. 1). It should be contrasted with correlators of local operators where analytic continuation from a constant time slice suffers from substantial (and natural) ambiguities related to the ordering of operators.

Finally, we want to acknowledge that earlier works that study the changes of entanglement entropy under rotations include Refs. [35,36]. While Ref. [35] focuses on spacelike slices, the results in Ref. [36] involve analogs of spacetime rotations in quantum spin chains in one spatial dimension. In particular, the latter indicates our prescription can be systematically studied in quantum many-body systems using tensor network methods or by focusing on Gaussian states.

III. HOLOGRAPHIC THERMAL STATE ON $\mathbb{R}^{1,2}$

In the present section, we employ the prescription advocated in Sec. II to interpret the multiple complex extremal surfaces from Ref. [28]. The paradigmatic setting in question consists of a four-dimensional black-brane spacetime and a strip subregion on the boundary (see Fig. 2). The holographic entanglement entropy for a strip subregion with $\theta=0$ is considered in Ref. [37], and the holographic timelike entanglement entropy candidate extremal surfaces for a strip subregion with $\theta=\pi/2$ is discussed in Ref. [28]. In the present section, we morph the results from $\theta=0$ into $\theta=\pi/2$ and show that, in the timelike regime, our prescription picks the extremal surfaces that fulfill the UV-IR correspondence. In particular, it will forbid one class of extremal surfaces from contributing for sufficiently small subregions.

A. Setup

The strip subregion of interest lives in the three-dimensional Minkowski spacetime located at the z=0 asymptotic boundary of the four-dimensional bulk geometry,

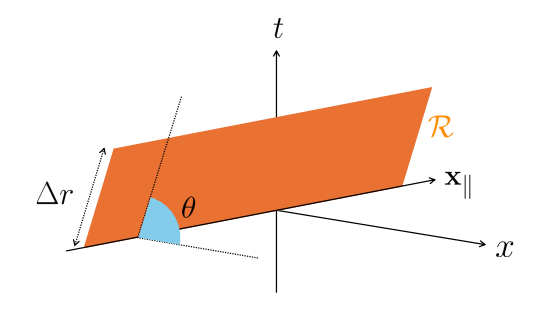


FIG. 2. Geometry of a strip boundary subregion \mathcal{R} in three-dimensional Minkowski space. The strip is rotated in the *t-x* plane, keeping the coordinate extent Δr fixed. See Fig. 1 for the case of a general subregion.

$$ds^{2} = \frac{1}{z^{2}} \left(\frac{dz^{2}}{f(z)} - f(z)dt^{2} + d\mathbf{x}^{2} \right), \tag{4}$$

where we have set the curvature scale to one. The choice f(z) = 1 corresponds to the empty anti–de Sitter (AdS) space, dual to the vacuum state of the boundary conformal field theory, whereas $f(z) = 1 - (z/z_H)^3$ corresponds to a black brane with the horizon located at $z = z_H$, dual to a thermal state.

Splitting the boundary spatial coordinates as $\mathbf{x} = \{x, x_{\parallel}\}$, the strip is defined as

$$\mathcal{R} \equiv \{(t, \mathbf{x}) : t = r \sin \theta, x = r \cos \theta, r \in [0, \Delta r], x_{\parallel} \in \mathbb{R} \},$$
(5)

where θ is fixed. The projection of the strip \mathcal{R} on the x-t plane is a segment joining the origin with the point $(\Delta r \cos \theta, \Delta r \sin \theta)$. The strip is spacelike for $\theta \in [0, \pi/4)$, null for $\theta = \pi/4$, and timelike for $\theta \in (\pi/4, \pi/2]$. The case considered in Ref. [28] corresponds to $\theta = \pi/2$. See Fig. 2 for an illustration of the setup.

By symmetry, the codimension-two bulk extremal surface γ_R takes the form

$$X^{\mu}(\lambda) = \{ z_s(\lambda), t_s(\lambda), x_s(\lambda), x_{\parallel} \}, \tag{6}$$

where λ is a parameter moving along the variable part of the surface. Given this result, we need to extremize the area density functional,

$$\mathcal{A} \equiv \frac{A}{V} \equiv \int d\lambda \mathcal{L} \equiv \int d\lambda \sqrt{\frac{\frac{z_s^2}{f(z_s)} - f(z_s)t_s'^2 + x_s'^2}{z_s^4}}, \quad (7)$$

to find the entropy density $S \equiv A/(4G_N)$. In this expression, V stands for the (formally infinite) volume of the line spanned by x_{\parallel} .

The area density in Eq. (7) is a UV-divergent quantity. In the following, we extract this UV divergence and work with the regularized area density

$$A_{\text{reg}} \equiv \lim_{\delta \to 0} \left(A - \frac{2}{\delta} \right), \tag{8}$$

where $\delta \ll 1$ corresponds to the location of the regularized asymptotic boundary in the radial direction of the bulk spacetime, $z = \delta$. Correspondingly, we also define

$$S_{\text{reg}} \equiv \frac{A_{\text{reg}}}{4G_N} \tag{9}$$

as the regularized entropy density.

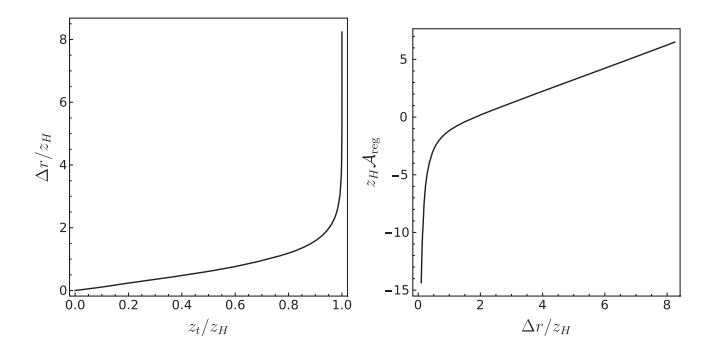


FIG. 3. Left panel: width of the strip Δr as a function of the position of the entangling surface tip z_t in the bulk spacetime. Right panel: regularized area density of the strip \mathcal{A}_{reg} as a function of the strip width Δr .

B. Holographic entanglement entropy for a horizontal strip

The calculation of the entanglement entropy of a space-like strip with $\theta=0$ is a standard problem in holography. One finds that, for a given width Δr , there is a single, real entangling surface. In the $\Delta r \to 0$ limit, the tip z_t of this entangling surface approaches the asymptotic boundary z=0, while in the opposite $\Delta r \to \infty$ limit, the tip approaches the black brane horizon $z=z_H$. Correspondingly, for $\Delta r \to 0$, the regularized entanglement entropy approaches its value in the vacuum state and diverges as Δr^{-1} , while for $\Delta r \to \infty$, it grows linearly in Δr with a slope governed by the location of the event horizon. See Fig. 3 for an illustration of these facts.

C. Holographic timelike entanglement entropy for a vertical strip

Reference [28] studied the holographic timelike entanglement entropy for timelike strips with $\theta=\pi/2$. One of the main findings of Ref. [28] was that the space of complex extremal surfaces associated with this boundary subregion comprises two classes of solutions, referred to as vacuum-connected and vacuum-disconnected solutions. Each class of solutions consists of two branches related to each other by complex conjugation. See Fig. 4 for the location of these branches in the complex z_t plane, with blue (green) curves denoting the location of the vacuum-connected (vacuum-disconnected) solutions. The regularized area density \mathcal{A}_{reg} of these solutions is shown later in Fig. 11, where we discuss the prediction of our holographic timelike entropy prescription.

The main properties of the vacuum-connected and vacuum-disconnected branches of complex extremal surfaces are as follows:

(i) For $\Delta r \to 0$, the tips of the vacuum-connected branches (blue curves in Fig. 4) flow to the location of the asymptotic boundary $z_t \to 0$, while the tips of the vacuum-disconnected ones (green curves in

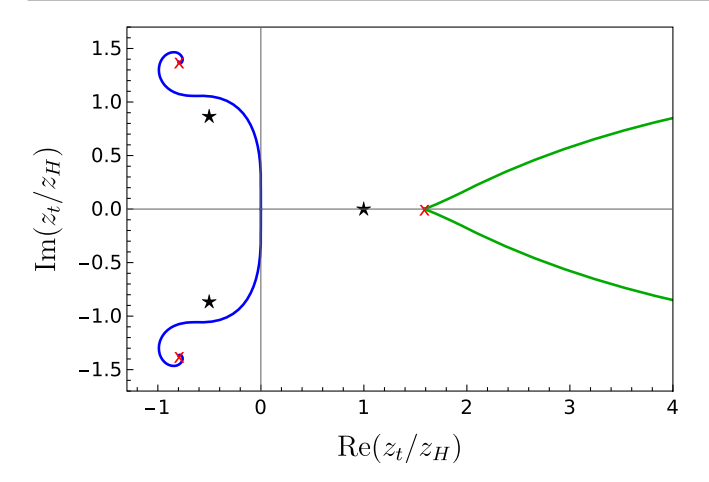


FIG. 4. For a strip with $\theta = \pi/2$, z_t for all the known complex extremal hypersurfaces in an AdS₄-Schwarzschild black brane. Blue (green) curves correspond to vacuum-connected (vacuum-disconnected) solutions. Horizons [understood as roots of f(z) = 0, see Eq. (4)] are represented as black stars, and critical extremal surfaces as red crosses. This plot appeared earlier in Ref. [28].

Fig. 4) flow to $|z_t| \to \infty$. Correspondingly, in the $\Delta r \to 0$ limit, the regularized area density of the vacuum-connected branches approaches the purely imaginary vacuum answer,

$$A_{\text{reg}} = i \frac{c_3}{\Delta r}, \qquad c_3 = \frac{4\pi\Gamma(\frac{3}{4})^2}{\Gamma(\frac{1}{4})^2}, \qquad (10)$$

while the regularized area density of the vacuumdisconnected ones goes to a complex constant with a negative real part, given by

$$\frac{2(-1+3^{\frac{1}{2}}i)\pi^{\frac{1}{2}}\Gamma(\frac{2}{3})}{\Gamma(\frac{1}{6})z_H}.$$
 (11)

We note that, in the vacuum case, there is a single complex extremal surface that can contribute to the timelike entanglement entropy. As shown in Ref. [28], the area density of this surface, given in Eq. (10), reproduces the holographic timelike entanglement entropy obtained from the analytic continuation of the closed-form expression for the entanglement entropy of a spacelike strip [18].

(ii) For $\Delta r \to \infty$, the tips of each branch flow to the location of a critical extremal surface for which $z_s(\lambda) = z_c \in \mathbb{C}$. From this observation, it follows that, in the $\Delta r \to \infty$ limit, the regularized area density of each branch grows linearly in Δr , with a slope determined by the corresponding critical extremal surface. The location z_c of the critical extremal surface is fixed by the requirement that the Lagrangian (7) evaluated on z_c is stationary [38],

$$\partial_{z_c} \sqrt{-\frac{f(z_c)}{z_c^4}} = 0. \tag{12}$$

In the case at hand, this equation allows for three solutions, one real and two complex conjugated: $z_1 = 2^{\frac{2}{3}}z_H$, $z_2 = 2^{\frac{2}{3}}e^{\frac{2\pi i}{3}}z_H$, and $z_3 = 2^{\frac{2}{3}}e^{-\frac{2\pi i}{3}}z_H$. These solutions are depicted as red crosses in Fig. 4; we clearly see that the vacuum-disconnected branches end in z_1 , while the upper (lower) vacuum-disconnected branch ends in z_2 (z_3). The $\Delta r \to \infty$ behavior of the regularized area density following from the location of the critical extremal surfaces is

$$\mathcal{A}_{\text{reg}}^{\text{v.c.}} \sim \frac{3^{\frac{1}{2}}}{2^{\frac{4}{3}}} e^{-\frac{i\pi}{3}} \frac{\Delta r}{z_H^2}, \qquad \mathcal{A}_{\text{reg}}^{\text{v.d.}} \sim \frac{3^{\frac{1}{2}}}{2^{\frac{4}{3}}} \frac{\Delta r}{z_H^2}.$$
 (13)

The key problem left open by Ref. [28] was how these different classes of complex extremal surfaces contribute to the holographic timelike entanglement entropy. In particular, note that minimizing over $\operatorname{Re} \mathcal{A}_{\operatorname{reg}}$ to select the dominant saddle would entail that, in the $\Delta r \to 0$ limit, the relevant solutions are the vacuum-disconnected ones; hence, the holographic timelike entanglement entropy thus defined does not reduce to the vacuum answer. Armed with the prescription put forward in Sec. II, we will return to this crucial question in Sec. III F below.

D. Entanglement entropy in the vicinity of the light cone

One of the key questions we have to address is how, under the analytic continuation described in Sec. II, the single branch of real extremal surfaces associated with a spacelike strip with $\theta=0$ gives way to the four branches of complex extremal surfaces associated with a timelike strip with $\theta=\pi/2$. To start answering this question, in this subsection, we explore the behavior of the holographic entanglement entropy when a spatial strip with $\theta<\pi/4$ approaches the null limit $\theta=\pi/4$.

Our first main result is that, as $\theta \to \pi/4$, past a critical angle θ_c , there exists a first-order phase transition in the entanglement entropy as Δr increases at fixed θ . At this first-order phase transition, the entangling surface $\gamma_{\mathcal{R}}$ changes discontinuously, and its tip z_t goes from being located close to the asymptotic boundary to being located close to the event horizon.

In the top panel of Fig. 5, we plot Δr as a function of z_t for values of θ progressively closer to $\pi/4$. We clearly see that, as $\varepsilon = \pi/4 - \theta \to 0$, Δr transitions from being a monotonic function of z_t to having a local maximum and a local minimum. Let the local maximum and minimum be associated with widths $\Delta r_{\max}(\varepsilon)$, $\Delta r_{\min}(\varepsilon)$ and tips $z_{t,\max}(\varepsilon)$, $z_{t,\min}(\varepsilon)$, respectively. These extrema naturally divide the entangling surface candidates into three branches:

 10^{-4}

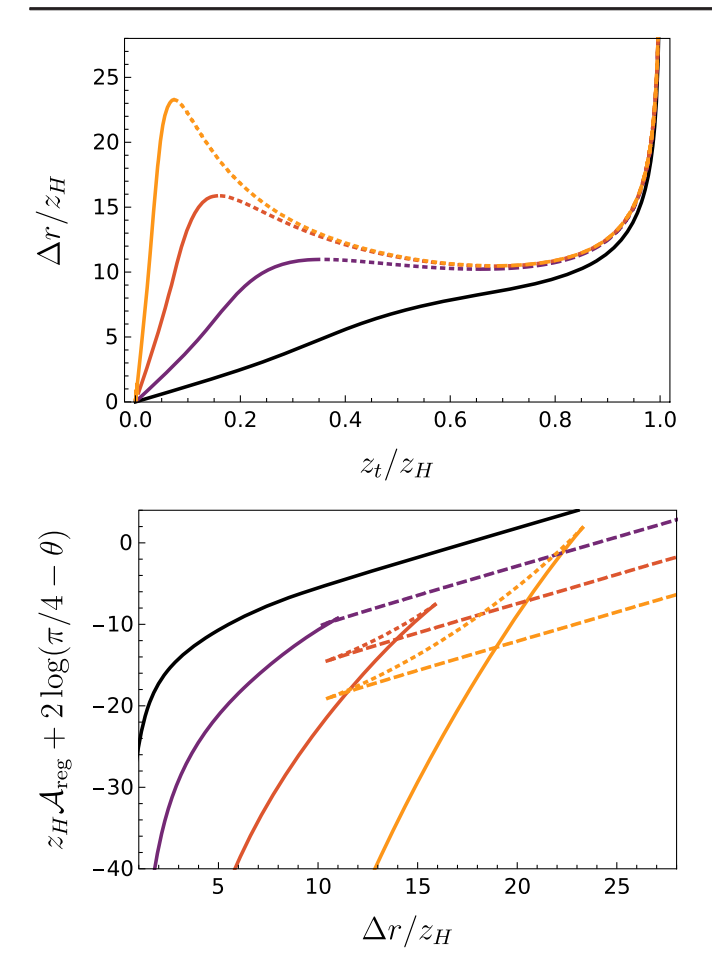


FIG. 5. Top panel: width of the strip Δr as a function of the tip of the extremal surface z_t for various values of $\theta = \cot^{-1}(1+\eta)$, where η represents the deviation from the light cone. Vacuum-connected, unstable, and horizon-connected branches for each θ correspond, respectively, to solid, dotted, and dashed lines. Bottom panel: regularized area density A_{reg} as a function of Δr for various angles. Each A_{reg} has been shifted by $\log[(\pi/4) - \theta]^2$ to prevent the curves from overlapping at large Δr .

- (i) Vacuum connected, with $0 \le z_t < z_{t,\max}(\varepsilon)$, depicted as solid curves.
- (ii) Unstable, with $z_{t,\max}(\varepsilon) \le z_t < z_{t,\min}(\varepsilon)$, depicted as dotted curves.
- (iii) Horizon connected, with $z_{t,\min}(\varepsilon) \le z_t < z_H$, depicted as dashed curves.

For strips with $\Delta r < \Delta r_{\min}(\varepsilon)$ or $\Delta r > \Delta r_{\max}(\varepsilon)$, there is a single extremal surface that can contribute to the entanglement entropy, while for strips with $\Delta r \in [\Delta r_{\min}(\varepsilon), \Delta r_{\max}(\varepsilon)]$, there are several. In the latter case, the holographic entanglement entropy prescription instructs us to select the one with the minimal area density, as all of them obey the homology constraint. As Δr increases, this competition leads to a first-order phase transition where the entangling surface jumps from the vacuum-connected branch to the horizon-connected one at a critical separation $\Delta r_c(\varepsilon) \in [\Delta r_{\min}(\varepsilon), \Delta r_{\max}(\varepsilon)]$. The unstable branch is always

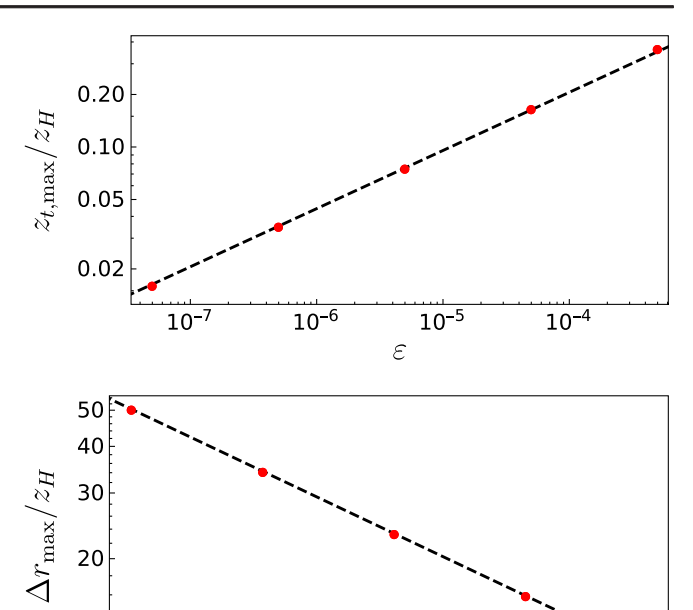


FIG. 6. Top panel: $z_{t,\max}/z_H$ as a function of ε (red dots) together with a fit to a $\varepsilon^{1/3}$ power law (black dashed line). Bottom panel: $\Delta r_{\max}/z_H$ as a function of ε (red dots) together with a fit to a $\varepsilon^{-1/6}$ power law (black dashed line).

 10^{-5}

ε

10⁻⁶

10-

subdominant. See the bottom panel of Fig. 5 for a plot of the regularized area density \mathcal{A}_{reg} as a function of Δr for various angles. The emergence of the swallowtail associated with the first-order phase transition as $\varepsilon \to 0^+$ is manifest from the plot.

Our numerical results are compatible with the fact that, as $\varepsilon \to 0$ and the null limit is approached, $z_{t,\min}(\varepsilon)$ and $\Delta r_{\min}(\varepsilon)$ saturate, while $z_{t,\max}(\varepsilon) \to 0$ and $\Delta r_{\max}(\varepsilon) \to \infty$. See Fig. 6 for a plot of $z_{t,\max}(\varepsilon)$ (top panel) and $\Delta r_{\max}(\varepsilon)$ (bottom panel), where we show that, in the $\varepsilon \to 0$ limit, these quantities behave as

$$\frac{z_{t,\max}(\varepsilon)}{z_H} \sim \varepsilon^{\frac{1}{3}}, \qquad \frac{\Delta r_{\max}(\varepsilon)}{z_H} \sim \varepsilon^{-\frac{1}{6}}. \tag{14}$$

These results imply that the window of widths for which a first-order phase transition is possible, $\Delta r \in [\Delta r_{\min}(\varepsilon), \Delta r_{\max}(\varepsilon)]$, is bounded from below and unbounded from above as $\varepsilon \to 0$. The critical width at which the phase transition itself takes place, $\Delta r_c(\varepsilon)$, also diverges in the same limit. For future reference, we define $\Delta r_{\min}^{\star} \equiv \lim_{\varepsilon \to 0} \Delta r_{\min}(\varepsilon) \approx 10.486z_H$. Note that, in light of these results, for a given Δr , it is always possible to pick θ sufficiently close to $\pi/4$ such that $\Delta r/\Delta r_c$ is arbitrarily small, z_t/z_H is arbitrarily close to zero, and, as a consequence, the regularized entanglement entropy S_{reg} is arbitrarily close to its vacuum value. This fact can be

understood as a manifestation of the UV-IR correspondence at the level of the entanglement entropy since, in the $\theta \to \pi/4^-$ limit, the proper width of a strip with fixed Δr goes to zero.

Finally, we point out that the first-order phase transition we have uncovered can be understood as emerging from a collision between real and complex branches of extremal surfaces. This fact follows from the observation that, even though for $\theta < \pi/4$ the boundary subregion is spacelike, there still exist complex-conjugated branches of complex extremal surfaces emanating from both $z_{t,\max}$ and $z_{t,\min}$. Moving away from $z_{t,\max}$ along these complex branches takes one to progressively larger $\Delta r \geq \Delta r_{\max}$, while moving away from $z_{t,\min}$ along them takes one to progressively smaller $\Delta r \leq \Delta r_{\min}$. Upon complexification of the angle θ , the branch collisions are resolved, and one finally obtains three smooth branches of extremal surfaces, which are now correspondingly complex. For $\operatorname{Im} \theta \to 0^-$, the branch rearrangement is as illustrated in Fig. 7:

- (i) The vacuum-connected branch of real extremal surfaces merges with the upper branch of complex extremal surfaces emanating from $z_{t,\max}$. The location of this complexified vacuum-connected branch in the complex z_t plane is depicted in blue in Fig. 7. The value of $z_{t,\max}$, where the leftmost branch collision took place, has been marked with an open circle.
- (ii) The lower branch of complex extremal surfaces emanating from $z_{t,\max}$, the unstable branch of real extremal surfaces, and the lower branch of complex extremal surfaces emanating from $z_{t,\min}$ all merge.

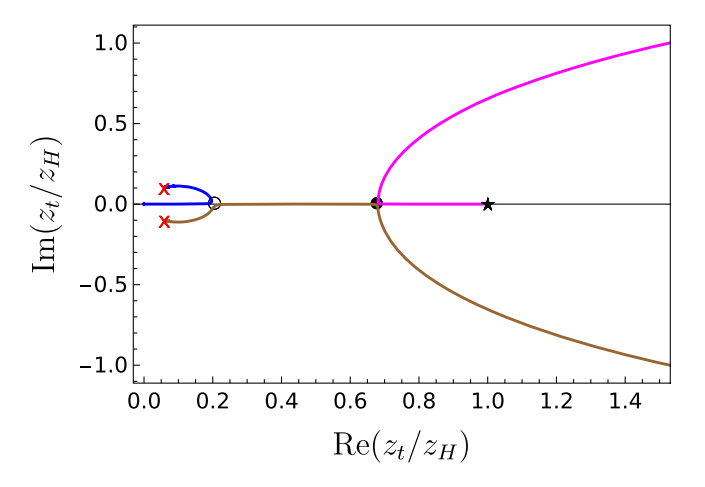


FIG. 7. Relevant branches of complex extremal surfaces for $\theta=\pi/4-10^{-4}-10^{-6}i$ as Δr is varied. The vacuum-connected, unstable, and horizon-connected branches of real extremal surfaces now, respectively, belong to the blue, brown, and magenta branches of complexified solutions. The event horizon is denoted by a black star, the location of $z_{t,\max}$ ($z_{t,\min}$) for $\theta=\pi/4-10^{-4}$ by open (filled) circles, and the tips of the critical extremal surfaces to which the complexified vacuum-connected and unstable branches flow as $\Delta r \to \infty$ by red crosses.

The location of this complexified unstable branch in the complex z_t plane is depicted in brown in Fig. 7. The value of $z_{t,min}$, where the rightmost branch collision took place, has been marked with a full circle.

(iii) The horizon-connected branch of real extremal surfaces merges with the upper branch of complex extremal surfaces emanating from $z_{t,min}$. The location of this complexified horizon-connected branch in the complex z_t plane is depicted in magenta in Fig. 7.

E. Analytical continuation past the light cone

According to the prescription put forward in Sec. II, to compute the timelike entanglement entropy of a strip with width Δr and tilt $\theta > \pi/4$, we first have to select the real extremal surfaces contributing to the entanglement entropy of a strip with the same width and $\theta = \pi/4 - 0^+$. Then, we analytically continue these real extremal surfaces around the light cone and finally pick among the resulting complex extremal surfaces the one with the smallest real part of the area density.

Our choice of analytical continuation is encapsulated in Fig. 1(b). We fix Δr and choose $\theta = \pi/4 - \varepsilon$ with $\varepsilon = 0^+$. Then, we set

$$\theta = \frac{\pi}{4} - \varepsilon e^{i\alpha},\tag{15}$$

keep ε fixed, and follow the initial real extremal surface as α goes from 0 to π . The end result is a complex extremal surface associated with a timelike strip with $\theta = \pi/4 + \varepsilon$. Finally, we follow this complex extremal surface as θ goes from $\pi/4 + \varepsilon$ to $\pi/2$. We carry out this procedure numerically by working with a small but finite ε . We note that, since for a given Δr it is always possible to choose ε sufficiently small so that $\Delta r < \Delta r_{\max}(\varepsilon)$, below we will only consider the cases where $\Delta r < \Delta r_{\min}(\varepsilon)$ and $\Delta r \in [\Delta r_{\min}(\varepsilon), \Delta r_{\max}(\varepsilon)]$.

In the case $\Delta r < \Delta r_{\min}(\varepsilon)$, only real extremal surfaces belonging to the vacuum-connected branch can contribute to the holographic entanglement entropy for $\theta \to \pi/4^-$. Our second main result is that, for this branch, the analytic continuation described above maps the initial real extremal surface at $\theta < \pi/4$ to a solution at $\theta = \pi/2$ that belongs to the upper vacuum-connected branch of complex extremal surfaces, depicted in blue in Fig. 4. Crucially, this implies that, for $\Delta r < \Delta r_{\min}(\varepsilon)$, the vacuum-disconnected branches of complex extremal surfaces at $\theta = \pi/2$, depicted in green in Fig. 4, do not correspond to the analytic continuation of real entangling surfaces and hence cannot contribute to the timelike entanglement entropy as we have defined it. This fact is critical for our holographic timelike entanglement entropy prescription to uphold the UV-IR correspondence.

As an illustration of these results, in Fig. 8, we show how the analytic continuation works in the $\varepsilon=10^{-4}$ case. In the top panel, we plot the trajectories traced in the complex z_t plane by the extremal surfaces with $\Delta r/z_H=1$, 2, 4, 6, 8, and 10, all smaller than $\Delta r_{\min}(10^{-4})/z_H\approx 10.44$, as θ varies along the path in Eq. (15). Each curve starts on the real axis at $\alpha=0$ and ends on a point with a nonzero imaginary part at $\alpha=\pi$, showcasing the complex nature of the extremal surface associated with the final timelike strip with $\theta=\pi/4+10^{-4}$. The bottom panel of Fig. 8 demonstrates that these complex surfaces, when θ is taken from $\pi/4+10^{-4}$ to $\pi/2$, always end up in the upper vacuum-connected branch of solutions shown in Fig. 4 and depicted in the bottom panel of Fig. 8 as a blue curve.

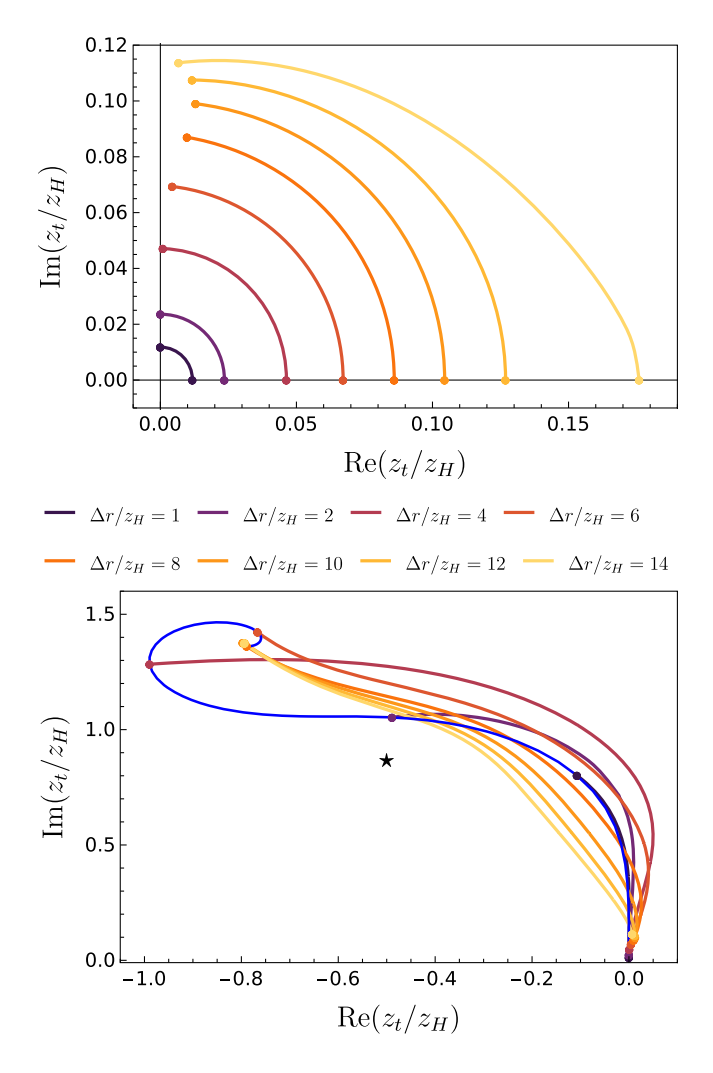


FIG. 8. Top panel: complex z_t -plane trajectories of extremal surfaces associated with strips with $\Delta r/z_H = 1, 2, 4, 6, 8, 10, 12$, and 14 and initial $\theta = \pi/4 + 10^{-4}$, as θ varies along the path in Eq. (15). Bottom panel: same as top panel, with θ going from $\pi/4 + 10^{-4}$ to $\pi/2$. The upper vacuum-connected branch of complex extremal surfaces at $\theta = \pi/2$ is depicted in blue as in Fig. 4. The black star corresponds to a complex black hole horizon.

In the case $\Delta r \in [\Delta r_{\min}(\varepsilon), \Delta r_{\max}(\varepsilon)]$, as $\theta \to \pi/4^-$, several real extremal surfaces can contribute to the entanglement entropy. Therefore, to identify the complex extremal surfaces relevant to the timelike entanglement entropy computation, we must consider the analytic continuation of not only the vacuum-connected branch of real extremal surfaces but also the unstable and horizon-connected ones.

In this range of Δr , the analytic continuation of the real saddles in the vacuum-connected branch proceeds analogously to the $\Delta r < \Delta r_{\rm min}(\epsilon)$ case. See the curves corresponding to $\Delta r/z_H=12$ and 14, all larger than $\Delta r_{\rm min}(10^{-4})/z_H$ and smaller than $\Delta r_{\rm max}(10^{-4})/z_H\approx 14.17$, in both the top and bottom panels of Fig. 8.

On the other hand, we find that, if we analytically continue around the light cone as in Eq. (15) and then take $\theta \to \pi/2$, real saddles in both the unstable and horizonconnected branches flow to the vacuum-disconnected branches of complex saddles depicted in Fig. 4. This finding is our third main result in this section. A subtlety arises for a fixed Δr as $\theta \to \pi/2$: at some intermediate angle $\theta_{\star} < \pi/2$, the solution originating from the unstable branch collides with the one from the horizon-connected branch. This collision makes it ambiguous to determine which solution connects to which vacuum-disconnected branch at $\theta = \pi/2$. To resolve this ambiguity, we introduce a small imaginary part to θ and define the branch assignment by taking the limit Im $\theta \to 0$, mirroring the discussion leading up to Fig. 7. Following this prescription, for $\text{Im } \theta < 0$, we find that solutions from the unstable (horizon-connected) branch flow to the lower (upper) vacuum-disconnected branch at $\theta = \pi/2$. For the choice Im $\theta = -10^{-6}$, this behavior is illustrated in Fig. 9, where we plot the trajectories traced in the complex z_t plane by the unstable (dashed curves, starting and ending in solid circles) and horizon-connected (solid curves, starting and ending in solid squares) complexified extremal surfaces as $Re\theta$ ranges from $\pi/4 - 10^{-4}$ to $\pi/2$. We have chosen the pairs of unstable and horizon-connected complexified extremal surfaces to be associated with widths $\Delta r/z_H =$ 11, 12, 13, and 14, all in between $\Delta r_{\text{max}}(10^{-4})/z_H$ and $\Delta r_{\rm min}(10^{-4})/z_H$. Note that these results explain why the vacuum-disconnected branches at $\theta = \pi/2$, originally found in Ref. [28], had to exist in the first place.

Our analysis so far has established that, for $\Delta r \in [\Delta r_{\min}(\varepsilon), \Delta r_{\max}(\varepsilon)]$, the complex saddles in the vacuum-disconnected branches at $\theta = \pi/2$ descend from real saddles in the pre-light-cone regime. It is natural to wonder where the remaining parts of these vacuum-disconnected branches come from. Given the results presented in Fig. 7, a natural guess is that, for $\Delta r < \Delta r_{\min}(\varepsilon)$, the vacuum-disconnected branches at $\theta = \pi/2$ descend from the pair of complex-conjugated branches of complex saddles emanating from $z_{t,\min}(\varepsilon)$, whose regularized version upon complexification of the angle θ can be found in Fig. 7.

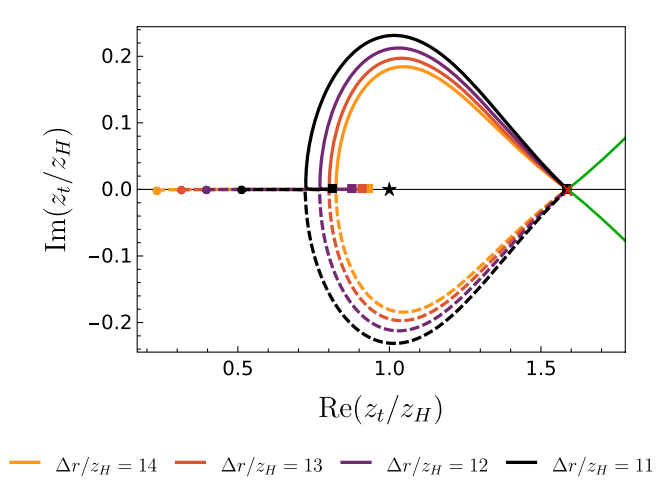


FIG. 9. For Im $\theta = -10^{-6}$, evolution in the complex z_t plane of four solutions with $\Delta r/z_H = 11$, 12, 13, and 14 in each of the complexified unstable (dashed curves) and horizon-connected branches (solid curves) as Re θ ranges from $\pi/4 - 10^{-4}$ to $\pi/2$. Clearly, solutions in the complexified unstable (horizon-connected) branch end in the lower (upper) vacuum-disconnected branch.

This expectation is confirmed by the results shown in Fig. 10. In this figure, we reproduce the complexified unstable (brown curve) and horizon-connected (magenta curve) branches at $\theta = \pi/4 - 10^{-4} - i10^{-6}$, originally depicted in Fig. 7, and plot the trajectories described by the complex extremal surfaces associated with widths $\Delta r/z_H = 3$, 4, 5, 6, 7, 8, 9, and 10 in the complex z_t plane as Re θ is increased to $\pi/2$, keeping Im θ fixed.

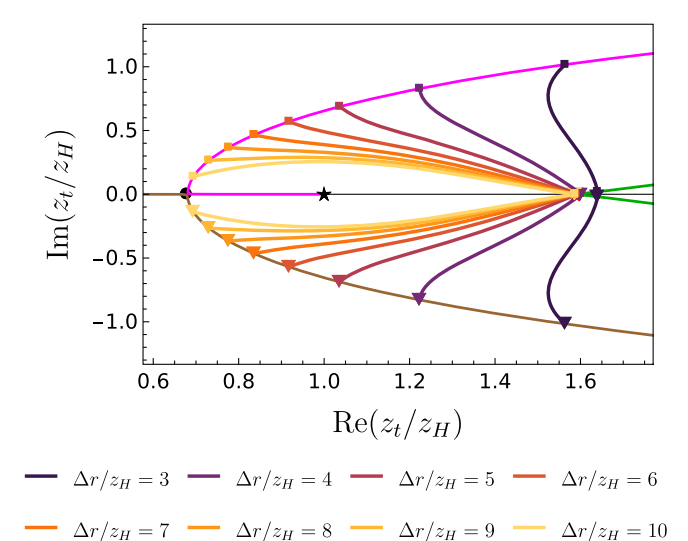


FIG. 10. For $\operatorname{Im}\theta=-10^{-6}$, evolution of the complexified unstable and horizon-connected branches at $\operatorname{Re}\theta=\pi/4-10^{-4}$ (cf. Fig. 7) as $\operatorname{Re}\theta\to\pi/2$. Clearly, the complexified unstable (horizon-connected) branch maps to the lower (upper) vacuum-disconnected branch at $\operatorname{Re}\theta=\pi/2$, shown here for $\operatorname{Im}\theta=0$ in green.

The trajectories corresponding to the complexified unstable (horizon-connected) solutions start and end at solid triangles (squares). As is manifest from the figure, at $\theta = \pi/2 - i10^{-6}$, every solution in the complexified unstable (horizon-connected) branch has moved to the lower (upper) vacuum-disconnected branch, depicted in green for the Im $\theta = 0$ case.

F. Area densities and timelike entanglement entropy

We are finally in a position to employ our prescription to compute the timelike entanglement entropy. We begin by examining the case $\theta = \pi/2$. The complex extremal surfaces have been shown in Fig. 4, and their corresponding area densities are provided in Fig. 11, with blue (green) curves corresponding to the vacuum-connected (vacuum-disconnected) result.

To evaluate the timelike entanglement entropy, we must consider two distinct regimes:

- (i) First, for $\Delta r < \Delta r_{\min}^{\star}$, our analysis from the previous subsection shows that only the complex extremal surfaces in the upper vacuum-connected branch contribute; hence, the timelike entanglement entropy computed according to our prescription upholds the UV-IR correspondence by construction.
- (ii) Second, for $\Delta r \geq \Delta r_{\min}^{\star}$, the vacuum-disconnected branches of complex extremal surfaces also become potential contributors, in addition to the upper vacuum-connected branch. We must choose the solution with the smallest real part of the area density. As shown in the top panel of Fig. 11, in this regime, the vacuum-disconnected branches always have a larger $\text{Re}\mathcal{A}_{\text{reg}}$ than the vacuum-connected branch. As a result, the upper vacuum-connected branch continues to dominate.

In conclusion, according to our prescription, the timelike entanglement entropy for a strip with $\theta=\pi/2$ is always determined by the upper vacuum-connected branch of complex extremal surfaces. In Fig. 11, we have highlighted this dominant contribution to the holographic timelike entanglement entropy with a dashed yellow line.

The computation of the timelike entanglement entropy for $\theta \in [\pi/4, \pi/2]$ proceeds in an analogous way, and the same conclusion follows, provided that for $\Delta r > \Delta r_{\min}^{\star}$ the area density of the vacuum-connected branch is lower than the rest. Empirically, we find that this is always the case except when θ is very close to $\pi/4$. In this immediate vicinity of the light cone, the vacuum-disconnected branches have smaller Re \mathcal{A}_{reg} than the vacuum-connected one at $\Delta r = \Delta r_{\min}^{\star}$ and, as a consequence, the timelike entanglement entropy features a zeroth-order phase transition as soon as the vacuum-disconnected complex extremal surfaces become available saddles. This zeroth-order phase transition gives way to a first-order phase transition at larger separations, where the vacuum-connected branch becomes dominant again. See Fig. 12

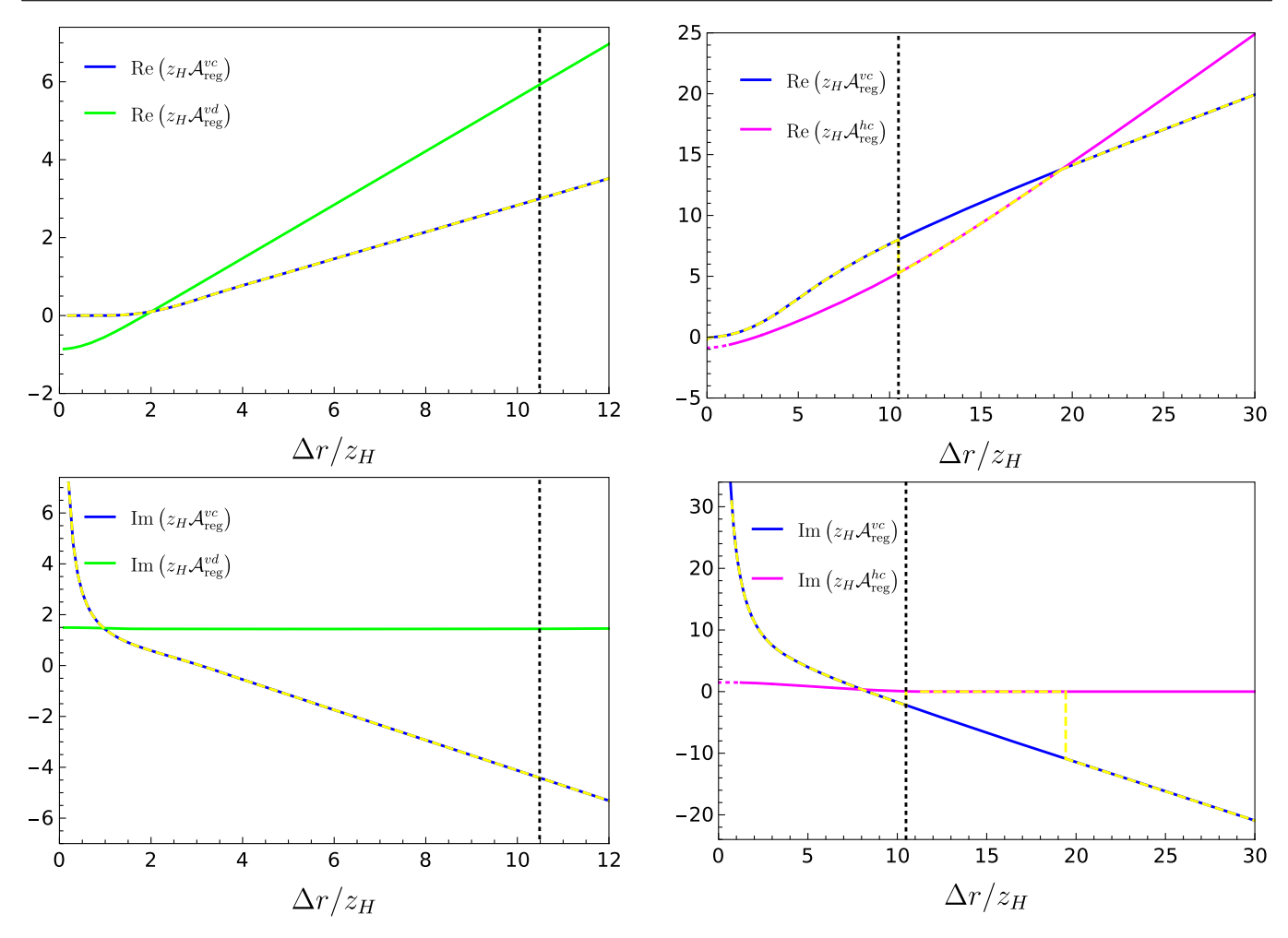


FIG. 11. Top panel: for a timelike strip with $\theta=\pi/2$, real part of the regularized area density \mathcal{A}_{reg} for the vacuum-connected (blue curve) and vacuum-disconnected (green curve) branches of extremal surfaces. The dotted vertical line marks the location of Δr_{\min}^{\star} , with the vacuum-disconnected branches becoming available saddles to its right. The dominant contribution to the real part of the timelike entanglement entropy according to our prescription has been highlighted with a yellow dashed line. Bottom panel: same as top panel, but for the imaginary part of the regularized area density of the upper vacuum-connected and vacuum-disconnected branches (the lower ones have the opposite value of Im \mathcal{A}_{reg}).

for an example with $\theta = \pi/4 + 0.002$. In this figure, the contributions of the analytical continuation of the vacuum-connected solutions are depicted in blue, while the contributions of the analytical continuation of the horizon-connected ones are depicted in magenta, just like in Fig. 7 (the analytical continuation of the unstable branch contribution is the complex conjugate of the horizon-connected one, and it is not shown to avoid clutter). Finally, the dominant contribution to the timelike entanglement entropy according to our prescription has been highlighted with a dashed yellow line, as in Fig. 11.

FIG. 12. Top panel: for a timelike strip with $\theta = \pi/4 + 0.002$, real part of the regularized area density \mathcal{A}_{reg} of the analytical continuation of the vacuum-disconnected (blue) and horizon-connected (magenta) branches (\mathcal{A}_{reg} for the analytical continuation of the unstable branch is the complex conjugate of the horizon-connected one, and it is not shown). The dotted part of the curves denotes that the corresponding quantity has been obtained through a numerical extrapolation. The dotted vertical line marks the location of Δr_{\min}^{\star} , and the dominant contributions to the timelike entanglement entropy according to our prescription have been highlighted in yellow. Interestingly, in this case, minimization of $\operatorname{Re} \mathcal{A}_{reg}$, together with connectedness to holographic entanglement entropy, induces a jump in $\operatorname{Re} \mathcal{A}_{reg}$. Bottom panel: same as top panel, but for the imaginary part of the regularized area density.

We conclude this section with two comments. The first is that, if we were to compute the timelike entanglement entropy by minimizing over *all* available complex extremal surfaces, we would find that, for a fixed θ , the vacuum-disconnected solutions dominate at sufficiently small Δr . Our analysis further shows that these vacuum-disconnected solutions for $\theta > \pi/4$ originate from complex saddles at $\theta < \pi/4$. Thus, the requirement that the timelike entanglement entropy preserves the UV-IR correspondence suggests that complex extremal surfaces should never be treated as

contributing subleading saddles in holographic entanglement entropy computations.

The second and final comment is that, given the presence of the zeroth-order phase transition in the timelike entanglement entropy in the immediate vicinity of the light cone, the reader might rightfully wonder why we have not decided to simply define the timelike entanglement entropy through the analytical continuation of the vacuum-connected branch of real extremal surfaces, which, for a given Δr , always gives the dominant contribution to the entanglement entropy infinitesimally before the light cone. In particular, note that this choice would also naturally uphold the UV-IR correspondence and, in addition, lead to a smooth answer for all angles. Our main reason for not pursuing this alternative definition is that in two-dimensional conformal field theories—where entanglement entropy is derived from a two-point correlator of twist operators—we expect the timelike entanglement entropy defined via analytic continuation of this correlator—to become singular whenever the insertion points are null separated. As we will show in the next section, our prescription naturally reproduces these null singularities, whereas the naive analytical continuation of the saddle that dominates immediately before the light cone does not.

IV. HOLOGRAPHIC THERMAL STATE ON $\mathbb{R} \times S^1$

We now show that, also in two-dimensional holographic conformal field theories with a compact spatial direction, the prescription advocated in the present paper and outlined in Sec. II gives a physically sensible result, as it correctly identifies the presence of light-cone singularities when the end points of the entangling region are null separated. Indeed, in two-dimensional conformal field theories, the entanglement entropy of a segment a is defined in terms of a two-point correlator of twist operators σ_n , $\bar{\sigma}_n$ evaluated at its end points, which implement the boundary conditions in the replica manifold [21],

$$S_a = \lim_{n \to 1} \frac{1}{1 - n} \log \langle \sigma_n \bar{\sigma}_n \rangle. \tag{16}$$

For a two-dimensional conformal field theory with a compact spatial direction ϕ in the vacuum state, Eq. (16) leads to

$$S_a = \frac{1}{4G_N} \log \left(\frac{4}{\delta^2} \sin \frac{\Delta t + \Delta \phi}{2} \sin \frac{\Delta t - \Delta \phi}{2} \right), \quad (17)$$

where Δt and $\Delta \phi$ are the coordinate differences between the end points of the entangling region and $\delta \ll 1$ is again a UV regulator [18,21]. The entropy in Eq. (17) is singular when the two end points are null separated, i.e., $\Delta t = \Delta \phi$, but also $\Delta t = 2\pi - \Delta \phi$. The latter condition arises due to the compact nature of the spatial direction and can be understood from the fact that, on a fixed spacetime slice,

any pair of points defines two intervals on the surface of the Lorentzian cylinder $\mathbb{R} \times S^1$, depending on the choice of leaving an end point clockwise or anticlockwise. As these singularities arise purely from geometrical properties of the boundary spacetime and do not depend on the bulk geometry, we will refer to them as kinematical singularities.

For this same reason, we expect such kinematical singularities to arise in thermal and excited states, as well. In these cases, the entanglement entropy for an interval cannot be expressed in closed form from the conformal field theory side. Still, it can be evaluated on the gravity side, where multiple competing configurations arise due to the presence of a nontrivial topological structure in the bulk (conical defect or black hole horizon). The goal of this section is to show that such divergences arise holographically only if the minimization over competing configurations, according to the prescription outlined in Sec. II, is applied after the analytic continuation through the light cone. Hence, this example further shows that the two operations, namely, selection of the dominant saddle by minimization and analytical continuation, do not commute, in general, emphasizing the need for the advocated prescription, which specifies their ordering.

A. Setup

We consider the family of three-dimensional bulk metrics parametrized by the real parameter $\mu \ge -1$,

$$ds^{2} = -(\rho^{2} - \mu)dt^{2} + \frac{d\rho^{2}}{\rho^{2} - \mu} + \rho^{2}d\phi^{2}, \qquad (18)$$

where $\rho \ge 0$, $\phi \in [0, 2\pi)$, and the asymptotic boundary where the dual conformal field theory lives is at $\rho \to \infty$. Comparing with Eq. (4), ρ plays the role of 1/z, and we use ρ as it is more convenient in the present setup.

All the geometries encapsulated by Eq. (18) represent the time development of states of two-dimensional conformal field theories on the Lorentzian cylinder $\mathbb{R} \times S^1$ of a unit radius. When $\mu = -1$, the line element in Eq. (18) represents the gravity dual to the vacuum state. If $-1 < \mu < 0$, it represents global AdS₃ with the insertion of a conical defect at $\rho = 0$, which corresponds to an excited state. Finally, if $\mu > 0$, the geometry in Eq. (18) describes the BTZ black hole [39], dual to the thermal state with temperature $T = \sqrt{\mu}/(2\pi)$.

B. Entanglement entropy on Cauchy slices

The entangling region of interest for this section is a single interval specified by a pair of boundary spacelike-separated points offset by Δt in time and $\Delta \phi$ in the angular direction. The entanglement entropy is then computed in terms of bulk geodesics connecting these points. For $\mu > -1$, i.e., in excited or thermal states, multiple geodesics exist that are enumerated by their winding number $n \geq 0$

around the conical defect at $\rho = 0$ (if $-1 < \mu < 0$) or the black hole horizon (if $\mu > 0$). All these different configurations should be considered as potential duals to the entanglement entropy. The geodesic connecting the region end points with winding number n = 0 has length

$$A = \log \left[\frac{2}{\mu \delta^2} (\cosh \Delta \phi \sqrt{\mu} - \cosh \Delta t \sqrt{\mu}) \right], \quad (19)$$

where we suppressed terms with positive powers of the UV regulator δ . When $-1 \le \mu < 0$, the hyperbolic functions become trigonometric ones; hence, the entropy has a periodicity that depends on the defect mass and coincides with the spatial one only in the vacuum $\mu = -1$. When $\mu > 0$, we have instead the typical linear behavior at large separations, which is expected in a thermal state. A sketch of such a geodesic in the case $\Delta t = 0$ is γ_0 in Fig. 13(a). A geodesic with generic winding number n has length given by Eq. (19) with $\Delta \phi \to 2\pi n - \Delta \phi$. Compare with γ_1 in Fig. 13(a) for a pictorial representation of the case with a single winding (n = 1).

If $\Delta t = 0$, i.e., the two points lie on the same constant time slice, the holographic entanglement entropy follows a well-known behavior: There exists a critical separation $\Delta \phi = \Delta \phi_*$ at which a phase transition occurs between the configuration γ_0 that does not wrap the defect (or the

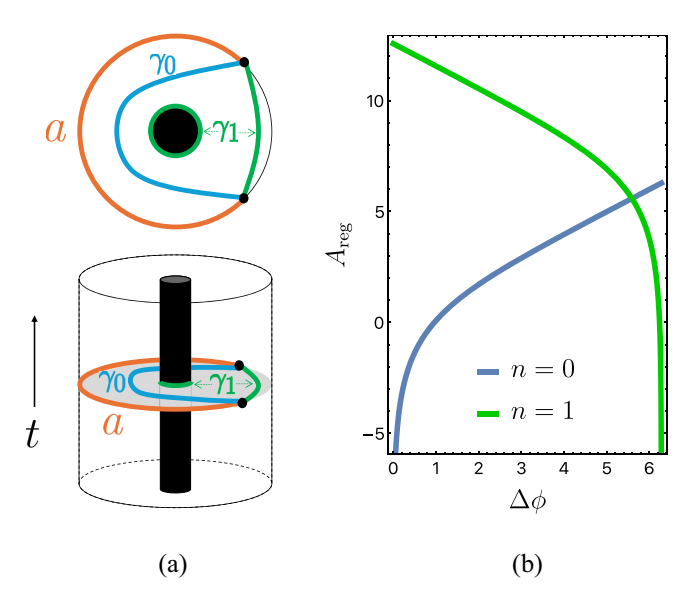


FIG. 13. (a) Sketch of two possible geodesics arising in the BTZ black hole metric given by Eq. (18) with $\mu > 0$, when the boundary interval a lies on a constant time slice: γ_0 (blue) with winding number n=0, and γ_1 (green) with n=1. Note that the latter includes an additional contribution around the black hole horizon to respect the homology constraint. Geodesics with a higher number of windings (not shown in the picture) also exist. (b) Regularized length $A_{\rm reg} \equiv A + 2\log\delta$ for the two geodesic configurations. While for small separations γ_0 dominates, there exists a value $\Delta\phi_* < 2\pi$ at which the two saddles exchange dominance.

horizon) and γ_1 that wraps the defect once. When $\Delta \phi > \Delta \phi_*$, the length of γ_1 becomes smaller than that of γ_0 [see Fig. 13(b)], and hence γ_1 dominates. Note that only the geodesics with the two lowest winding numbers n = 0, 1 are the ones that exchange dominance under the criterion of selecting the one with minimal length [40].

When there is a black hole horizon in this setup, the homology constraint plays a crucial role. The homology constraint consists of the requirement that there exists a codimension-one interpolating homology surface whose only boundaries are the entangling surface γ and the boundary subregion a. It is usually motivated by the fact that the causal wedge of the boundary subregion has to be contained within its entanglement wedge [41]. As a consequence, when $\mu > 0$, the wrapping configuration γ_1 includes a contribution coming from a disconnected piece encircling the horizon [see Fig. 13(a)].

These considerations apply equally to intervals that lie on tilted spacetime slices, i.e., whose end points are separated by $\Delta \phi$ along the spatial direction and Δt along time, provided that the two end points are spacelike separated,

$$\Delta t < \min\left(\Delta\phi, 2\pi - \Delta\phi\right),\tag{20}$$

where the term $2\pi - \Delta \phi$ originates from the compactness of the spatial circle giving rise to two ways of connecting a pair of points. Note that the condition in Eq. (20) can be understood as the condition for the existence of a global spatial (time) slice containing the subregion or, in other words, by demanding that the complement is also spatial. We will be interested in these more general tilted subsystems, as they are intermediate steps in the analytic continuations being part of our prescription for holographic timelike entanglement entropy.

When the condition in Eq. (20) is satisfied, the bulk extremal surfaces (here, geodesics) are real and hence potential contributors to the standard entanglement entropy. The homology constraint is also understood in the same manner as on the constant time slice considered above.

When the inequality in Eq. (20) saturates, then either a subregion or its complement becomes null. This limit is singular for entanglement entropy, and we will analytically continue across it using our prescription (see Fig. 1).

C. Analytic continuation past the light cone

In the following, we employ the prescription outlined in Sec. II in the three-dimensional bulk setup of Eq. (18). We utilize

$$\Delta \phi = \Delta r \cos \theta$$
 and $\Delta t = \Delta r \sin \theta$. (21)

There are three key differences with respect to the case studied in Sec. III, both originating from the compactness of the spatial direction:

- (i) The maximal value of Δr that we can take, starting with entanglement entropy, is naturally limited by 2π . As a result, the outcome of the prescription outlined in Sec. II at any value of the rotation angle—in particular, at its maximal value $\theta = \pi/2$ —will be limited to $\Delta r = 2\pi$. While in the tensor network picture of temporal entanglement there does not seem to be a need for such a limitation, in this section, we just accept it as a feature of the prescription relying on the analytic continuation depicted in Fig. 1, and in Sec. V, we will speculate on how to go beyond $\Delta r = 2\pi$.
- (ii) The compact nature of the spatial direction leads to the appearance of null singularities not only at $\theta = \pi/4$ but also at the other values of θ when the points become connected via a null geodesics going across the other side of the cylinder (see Fig. 14). Which one is hit first depends on the value of Δr :
 - $\Delta r < (1/\sqrt{2}) \times 2\pi$: In this case, the rotation encounters only the familiar light-cone singularity when the subregion itself becomes null at $\theta = \pi/4$. This singularity is avoided by a small detour into the complex θ plane as in Fig. 1. The subsequent rotation to the timelike regime of $\pi/4 < \theta \le \pi/2$ does not encounter any additional singularities as the complement remains spacelike, compare with Fig. 14.
 - $(1/\sqrt{2}) \times 2\pi < \Delta r < 2\pi$: Full rotation to $\theta = \pi/2$ encounters three null singularities (see Fig. 14). The first one, θ_1 , is associated with the complement becoming null, and only for θ smaller than this threshold value does the notion of entanglement

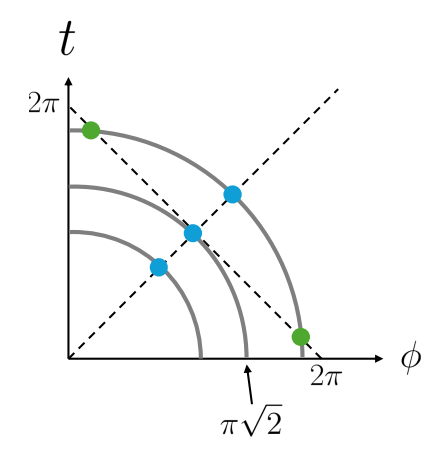


FIG. 14. Emergence of null singularities along the rotation in Eq. (21) as a function of the boundary interval size Δr . There is a critical value $\Delta r = \pi \sqrt{2}$ below which only the singularity at $\theta = \pi/4$ appears in the configuration with n=0 (blue dots). For $\Delta r > \pi \sqrt{2}$, instead, two more kinematical singularities arise when the end points are null separated by hitting the light cone emitted by the other end point (green dots, compare with Figs. 15–17 for a plot of the divergences).

entropy still apply. The second null singularity is associated with the subregion itself becoming null and is still at $\theta_2 = \pi/4$. The third one, θ_3 , is associated with the complement becoming null again. The kinematical singularities arising from the complement becoming null do not depend on the state and are given by

$$\theta_{1,3} = \arctan \frac{2\pi \mp \sqrt{2}\sqrt{\Delta r^2 - 2\pi^2}}{2\pi \pm \sqrt{2}\sqrt{\Delta r^2 - 2\pi^2}}.$$
 (22)

We deal with all these null singularities by the excursion onto the complex θ plane, as in Fig. 1, but at the respective real values of the angle.

(iii) Whereas in Sec. III all real extremal surfaces in the spatial regime satisfied the homology constraint, this is no longer the case here for $\mu > 0$, which has to be taken into account before the analytic continuation past the first light cone takes place.

Below, we discuss each class of solutions one by one, as well as the emerging picture for the holographic timelike entanglement entropy. We always consider the regime $\Delta r > \pi \sqrt{2}$, where all the kinematical singularities arise, which will be a crucial element in testing our prescription.

- (i) Vacuum ($\mu = -1$): In the case of the empty AdS₃ geometry, there is only one extremal surface for each pair of points specifying the subregion and its complement. When both the subregion and its complement are spatial, the surface is real and trivially satisfies the homology constraint. The analytic continuation past each singularity is therefore unique and does not carry any ambiguity. See Fig. 15 for an example.
- (ii) Conical defect $(-1 < \mu < 0)$: In this case, multiple configurations arise depending on their winding number n around the conical defect. They feature not only the kinematical singularities in Eq. (22) but also bulk singularities associated with null connectivity over the bulk; see, e.g., Refs. [42–45] for corresponding discussions in the context of boundary correlation functions. Bulk singularities depend on the structure of the dual spacetime, in this case, on the mass of the defect μ . As can be seen from Fig. 16, bulk singularities arise up to a given winding number, which also depends on the value of μ . The homology constraint is again automatically satisfied, as the minimal contour encircling the defect has zero measure. However, the analytic continuation is no longer unique, as when crossing each singularity as described in Sec. II, there is an ordering ambiguity between crossing the light cone and selecting the configuration with a minimal real part. This issue will be addressed at the end of this section, showing that the prescription described in Sec. II solves this ambiguity coherently with field theory expectations.

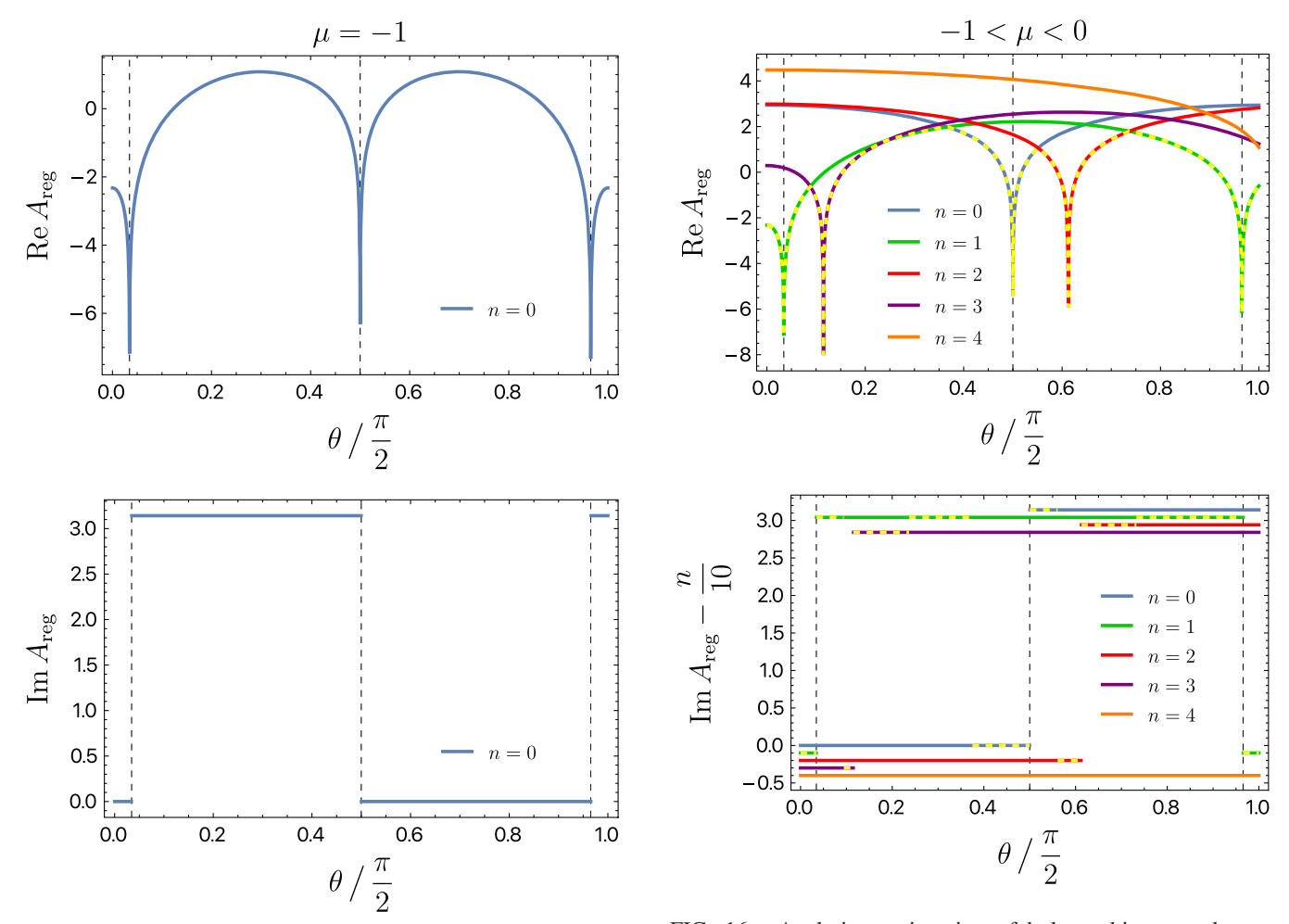


FIG. 15. Analytic continuation of holographic entanglement entropy in the vacuum state, $\mu=-1$. The size of the boundary interval $\Delta r=1.9\pi$ is fixed to be larger than the critical value $\pi\sqrt{2}$ past which additional kinematical singularities appear, and we vary θ from 0 (constant time slice) to $\pi/2$. Only the configuration n=0 contributes in this case. Top panel: real part, which exhibits the kinematical singularities. Bottom panel: imaginary part plotted modulo 2π , which assumes the value 0 or π depending on the end points being spacelike or timelike separated.

(iii) BTZ black hole ($\mu > 0$): In this case, as expected, the same kinematical singularities as in Eq. (22) arise; see Fig. 17. An additional complication with respect to the conical defect case is the homology constraint, which now has to be carefully enforced at any value of θ . As discussed before, on constant time slices, the contribution from the homology constraint is typically taken to be the length of a curve wrapping the horizon, i.e., $2\pi\sqrt{\mu}$, for any geodesic that wraps the horizon an odd number n of times. Intuitively, this condition emerges from the fact that a geodesic with n even always has a piece around the horizon that acts as a "screen" for the others, ensuring the existence of an interpolating surface between the extremal surface and the boundary

FIG. 16. Analytic continuation of holographic entanglement entropy in the excited state dual to AdS_3 with insertion of a conical defect, $-1 < \mu < 0$. The size of the boundary interval is $\Delta r = 1.9\pi$, as in Fig. 15. Depending on the value of the defect mass μ , additional bulk singularities arise on top of the kinematical ones that were already apparent in the vacuum state of Fig. 15. The value of μ also determines which configurations contribute to the entropy: In this case, we chose the value $\mu = -0.2$ to avoid clutter, and geodesics with $n \le 3$ are relevant. The dominant configurations selected by minimization are highlighted in yellow. Top panel: real part. Bottom panel: imaginary part plotted modulo 2π , which still assumes the two discrete values 0 and π . An n-dependent shift has been introduced for readability.

subregion required to satisfy the homology constraint. This is not the case for n odd, as the innermost part of the curve will always need a further screen from an additional piece encircling the horizon; see Fig. 13.

We now show how our prescription addresses the kinematical singularities, focusing on the last two cases (conical defect and BTZ black hole, $\mu > -1$), where ambiguities in the analytical continuation arise due to the existence of multiple extremal surfaces (here, geodesics). Consider the first kinematical singularity θ_1 .

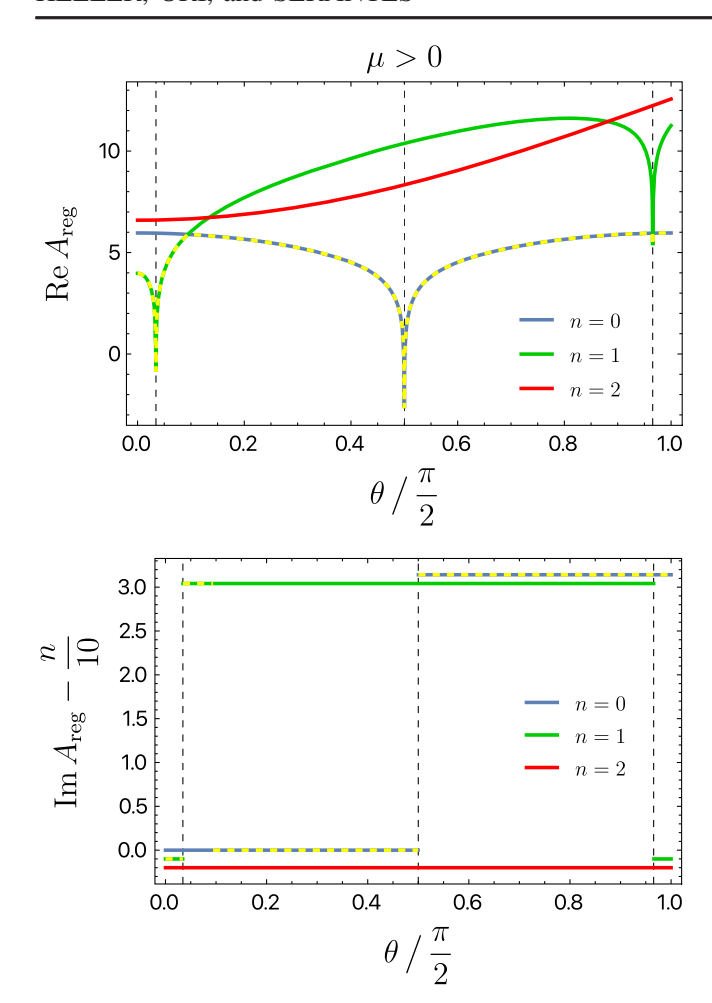


FIG. 17. Analytic continuation of holographic entanglement entropy in the thermal state dual to the BTZ black hole, $\mu > 0$. The size of the boundary interval is $\Delta r = 1.9\pi$, as in Figs. 15 and 16, and $\mu = 1$. In this case, only geodesics with n < 2 contribute to the entropy. The homology constraint is enforced for the configuration n = 1 by adding the horizon length $2\pi\sqrt{\mu}$. The dominant configurations are highlighted in yellow. Top panel: real part. Bottom panel: imaginary part plotted modulo 2π , which still assumes the two discrete values 0 and π . An n-dependent shift has been introduced for readability.

According to the prescription of Sec. II, the entropy for $\theta > \theta_1$ is defined by analytical continuation of all the real geodesic configurations at $\theta = 0$ up to θ , and then by selecting the configuration with the smallest real part. Thus, the minimization at θ occurs *after* crossing the light cone at θ_1 . Keeping only the saddle with a minimal real part *before* crossing the singularity at θ_1 , instead, does not allow us to reproduce the next singularities $\theta_i > \theta_1$, as they can arise from saddles that are not dominating at θ_1 . This result occurs whenever there is an exchange of dominance between different saddles after the singularity θ_1 , which is often the case (compare with Figs. 15 and 16). The same argument applies for all the other singularities, θ_i .

As a concrete example, consider, again, Figs. 15 and 16 and focus on the kinematic singularities. An exchange of

dominance arises between the configurations n=0 and n=1 as a function of θ . Let us consider, for instance, the singularity $\theta_2=\pi/4$ (any other singularity would lead to the same result). Even if for $\theta=0$ the configuration with winding number n=1 dominates (which is the case both for the conical defect and the BTZ black hole), as the light cone is approached, there is a phase transition such that when $\theta\to\pi/4^-$ the dominant configuration will always be the one with n=0. Indeed, in this limit, the lengths in Eq. (19) are approximated by

$$A = \log \left[\frac{2}{\mu \delta^2} \left(\cosh \sqrt{\mu} \left(2n\pi - \frac{\Delta r}{\sqrt{2}} \right) - \cosh \Delta r \sqrt{\frac{\mu}{2}} \right) \right] + \mathcal{O}\left(\theta - \frac{\pi}{4} \right).$$
 (23)

Clearly, in the $\theta \to \pi/4^-$ limit, the dominant configuration for any value of Δr is given by the geodesic with no windings n=0, as the length above diverges to $-\infty$ while the others remain finite. From this kind of limit, it is always possible to show that when a configuration with given n diverges, the others remain finite; hence, minimization after crossing the light cone will always pick the one exhibiting the kinematical divergence. Finally, note that there can also be light-cone divergences for fine-tuned values of $\Delta r = n\pi\sqrt{2}$ such that the n-windings configuration is equally divergent to $-\infty$. This case does not affect the statement that, in general, the dominant configuration does not correspond to the one leading to the expected light-cone singularities in the timelike regime.

As a consequence, if timelike entanglement entropy is defined through the analytic continuation of the saddle giving the dominant contribution to the entanglement entropy immediately *before* crossing the first null singularity θ_1 , a geodesic with the same winding number will dominate for any $\theta > \theta_1$ (compare with Figs. 15 and 16), and the next null singularities at $\theta_i > \theta_1$ will not be detected. This observation shows that the saddle giving the dominant contribution to the timelike entanglement entropy after a null singularity has to be chosen by minimizing the real part of the length *after* performing the analytical continuation of the relevant geodesic configurations across the light cone, which provides further support for the prescription outlined in Sec. II, as already anticipated at the end of Sec. III F.

V. OUTLOOK

A significant portion of our understanding of quantum field theory phenomena occurring at temporal separations, such as subsequent measurements or the response of a system to a local perturbation, is based on analytic continuations of operator insertions in correlation functions away from a Cauchy slice (constant time slice in some foliation). In the present paper, building on earlier

developments in Refs. [17,18], we applied the same principle to entanglement entropy in quantum field theory and defined the temporal entanglement by means of an analytic continuation of an entangling region to acquire a temporal extent. Our analytic continuation can be thought of as a generalization of a kinematic space research program (see Refs. [46–49]), which studies entanglement entropy dependence on the shape and location of the subregion, including how it changes as a function of both space and time.

Within the kinematic space paradigm to date, the subregions of interest (together with their complements to be able to define a state) were bound by light cones. In the present work, we propose to *define* temporal entanglement entropy in Minkowski spacetimes in terms of a spacetime transformation encapsulated in Fig. 1. The transformation in question needs to be complexified in order to go past the light cone. This spacetime rotation, when applied to known closed-form expressions for entanglement entropy, reproduces the results of Refs. [17,18].

However, given the scarceness of exact expressions for entanglement entropy, the key power of our idea lies in its applicability to holography, where entanglement entropy calculations amount to studying extremal surfaces in higher-dimensional spacetimes. Within our approach, all extremal surfaces that could contribute to holographic entanglement entropy are analytically continued following the change of the asymptotic boundary condition encapsulated by Fig. 1. The holographic timelike entanglement entropy is then computed by the resulting complex extremal surface with the smallest real part of the area.

Our holographic investigations resolve the puzzle posed in Ref. [28] regarding which complex extremal surface should be chosen as the dominant contribution to holographic timelike entanglement entropy when multiple candidates exist. We find that, among the complex extremal surfaces obtained via analytic continuation of those relevant for holographic entanglement entropy, the correct choice is the one that minimizes the real part of the area. Interestingly, the minimization aspect of our construction leads to strong subadditivity of holographic timelike entanglement entropy provided the real part of all involved surfaces is nonzero. It would be very interesting to understand if this subadditivity is a feature of holographic setups or extends to the analytic continuation of entanglement entropy in general quantum field theories.

More along these lines, we also uncovered a lesson about holographic entanglement entropy itself: Self-consistency of our prescription requires us not to consider complex extremal surfaces as possible subleading (in the real part of the area) contributions to holographic entanglement entropy.

While in the present paper we studied two holographic setups that were chosen to test different aspects of our key idea, the prescription we outlined here is already made to undertake a comprehensive exploration of temporal entanglement across the whole holographic entanglement entropy landscape. Such studies would allow us to uncover detailed properties of holographic timelike entanglement entropy and, in particular, could lead to identifying phenomena for which it arises as a natural quantity to consider. The perspective that we have in mind originates from the physics of correlation functions. For example, while it is true that the shear viscosity of a quantum field theory in its thermal state is encoded in a Euclidean correlator of the energy-momentum tensor, it is much easier to access it from an analytically continued correlator: the retarded one. Although unknown to us at the moment, we expect there are phenomena for which timelike entanglement entropy is, in a similar vein, more natural to consider than the entanglement entropy itself.

Another interesting aspect of our construction for future studies is the connection with the notion of temporal entanglement pursued in Ref. [50]. We believe this connection manifests itself in the two-dimensional conformal field theory setup on a Lorentzian cylinder considered in Sec. III. Our prescription, as it stands, does not allow us to define temporal entanglement entropy for intervals of larger extent in time than the circumference of the cylinder, as this is the largest possible size of a spatial interval giving rise to a standard notion of a state in quantum field theory. However, if one were to consider spatial intervals wrapping along the cylinder and of arbitrary length, then their analytic continuation could be used as a definition of timelike entanglement entropy for timelike intervals of arbitrary extent. Upon a slight boost, such spatial intervals of arbitrary lengths are reminiscent of the approach of Ref. [50], as they would be spacelike subregions containing, nevertheless, timelike separated points.

Finally, it would be very interesting to study the analytic continuation pursued in the present paper from the perspective of quantum many-body systems giving rise to relativistic quantum field theories at low energies. For example, while the kinematic singularities encountered in Sec. IV should also be present in a regularized way on a lattice (as they are associated with the causal structure of the spacetime in which the quantum field theory lives), what we identified as the bulk singularities should not be present in a general, discrete, quantum many-body system. Therefore, such studies have the potential of understanding which features of timelike entanglement entropy in computable examples are holography specific and which ones might be more general and, perhaps, amenable to a general-level proof or a higher-level physical argument.

Note added. Recently, we became aware of the results of Nunez and Roychowdhury [51], who also explored spacelike-to-timelike analytic continuations to define timelike entanglement entropy in holography.

ACKNOWLEDGMENTS

We would like to thank Hong Liu, Alexey Milekhin, Luca Tagliacozzo, and Tadashi Takayanagi for discussions on the topic of temporal entanglement, Rob Myers for discussions and making us interested in the case studied in Sec. IV, Carlos Nunez and Dibakar Roychowdhury for sharing with us their related results before they were online, and Meng-Ting Wang for comments on the draft. This project has received funding from the European Research Council (ERC) under the European Union's Horizon 2020 research and innovation programme (Grant No. 101089093, project acronym: High-TheQ). This work was partially supported by the Priority Research Area Digiworld under the program Excellence Initiative—Research University at the Jagiellonian University in Krakow. F.O. is supported by the Research Foundation Flanders (FWO) Doctoral Fellowship No. 1182825N. M. P. H. would like to acknowledge the hospitality of Nordita during the completion of this work. Published with partial support from the Belgian University Foundation.

Views and opinions expressed are those of the authors only and do not necessarily reflect those of the European Union or the European Research Council. Neither the European Union nor the granting authority can be held responsible for them.

DATA AVAILABILITY

No data were created or analyzed in this study.

- [1] R. Orus, A practical introduction to tensor networks: Matrix product states and projected entangled pair states, Ann. Phys. (Amsterdam) **349**, 117 (2014).
- [2] J. I. Cirac, D. Perez-Garcia, N. Schuch, and F. Verstraete, Matrix product states and projected entangled pair states: Concepts, symmetries, theorems, Rev. Mod. Phys. 93, 045003 (2021).
- [3] B. Zeng, X. Chen, D.-L. Zhou, and X.-G. Wen, Quantum Information Meets Quantum Matter: From Quantum Entanglement to Topological Phases of Many-Body Systems, Quantum Science and Technology (Springer, New York, 2019)
- [4] T. Mori, T. N. Ikeda, E. Kaminishi, and M. Ueda, *Thermalization and prethermalization in isolated quantum systems: A theoretical overview*, J. Phys. B **51**, 112001 (2018).
- [5] J. Berges, M.P. Heller, A. Mazeliauskas, and R. Venugopalan, QCD thermalization: Ab initio approaches and interdisciplinary connections, Rev. Mod. Phys. 93, 035003 (2021).
- [6] H. Casini and M. Huerta, Lectures on entanglement in quantum field theory, Proc. Sci., TASI2021 (2023) 002.
- [7] T. Nishioka, S. Ryu, and T. Takayanagi, *Holographic entanglement entropy: An overview*, J. Phys. A **42**, 504008 (2009).

- [8] M. Rangamani and T. Takayanagi, *Holographic Entanglement Entropy*, (Springer, New York, 2017), Vol. 931.
- [9] B. Chen, B. Czech, and Z.-z. Wang, *Quantum information in holographic duality*, Rep. Prog. Phys. **85**, 046001 (2022).
- [10] A. Almheiri, T. Hartman, J. Maldacena, E. Shaghoulian, and A. Tajdini, *The entropy of Hawking radiation*, Rev. Mod. Phys. 93, 035002 (2021).
- [11] M. C. Bañuls, M. B. Hastings, F. Verstraete, and J. I. Cirac, Matrix product states for dynamical simulation of infinite chains, Phys. Rev. Lett. 102, 240603 (2009).
- [12] M. B. Hastings and R. Mahajan, Connecting entanglement in time and space: Improving the folding algorithm, Phys. Rev. A 91, 032306 (2015).
- [13] M. Frías-Pérez and M. C. Bañuls, Light cone tensor network and time evolution, Phys. Rev. B 106, 115117 (2022).
- [14] A. Lerose, M. Sonner, and D. A. Abanin, *Overcoming the entanglement barrier in quantum many-body dynamics via space-time duality*, Phys. Rev. B **107**, L060305 (2023).
- [15] G. Giudice, G. Giudici, M. Sonner, J. Thoenniss, A. Lerose, D. A. Abanin, and L. Piroli, *Temporal entanglement*, quasiparticles, and the role of interactions, Phys. Rev. Lett. 128, 220401 (2022).
- [16] S. Carignano, C. R. Marimón, and L. Tagliacozzo, *Temporal entropy and the complexity of computing the expectation value of local operators after a quench*, Phys. Rev. Res. **6**, 033021 (2024).
- [17] K. Doi, J. Harper, A. Mollabashi, T. Takayanagi, and Y. Taki, *Pseudoentropy in dS/CFT and timelike entanglement entropy*, Phys. Rev. Lett. **130**, 031601 (2023).
- [18] K. Doi, J. Harper, A. Mollabashi, T. Takayanagi, and Y. Taki, *Timelike entanglement entropy*, J. High Energy Phys. 05 (2023) 052.
- [19] K. Narayan, De Sitter space, extremal surfaces, and time entanglement, Phys. Rev. D 107, 126004 (2023).
- [20] C. Holzhey, F. Larsen, and F. Wilczek, Geometric and renormalized entropy in conformal field theory, Nucl. Phys. B424, 443 (1994).
- [21] P. Calabrese and J. L. Cardy, Entanglement entropy and quantum field theory, J. Stat. Mech. (2004) P06002
- [22] S. Carignano and L. Tagliacozzo, Loschmidt echo, emerging dual unitarity and scaling of generalized temporal entropies after quenches to the critical point, Quantum 9, 1859 (2025).
- [23] S. Ryu and T. Takayanagi, *Holographic derivation of entanglement entropy from AdS/CFT*, Phys. Rev. Lett. **96**, 181602 (2006).
- [24] V. E. Hubeny, M. Rangamani, and T. Takayanagi, A covariant holographic entanglement entropy proposal, J. High Energy Phys. 07 (2007) 062.
- [25] H. Casini, M. Huerta, and R. C. Myers, *Towards a deriva*tion of holographic entanglement entropy, J. High Energy Phys. 05 (2011) 036.
- [26] A. Lewkowycz and J. Maldacena, Generalized gravitational entropy, J. High Energy Phys. 08 (2013) 090.
- [27] X. Dong, A. Lewkowycz, and M. Rangamani, *Deriving covariant holographic entanglement*, J. High Energy Phys. 11 (2016) 028.
- [28] M. P. Heller, F. Ori, and A. Serantes, *Geometric interpretation of timelike entanglement entropy*, Phys. Rev. Lett. **134**, 131601 (2025).

- [29] L. Fidkowski, V. Hubeny, M. Kleban, and S. Shenker, *The black hole singularity in AdS/CFT*, J. High Energy Phys. 02 (2004) 014.
- [30] V. Balasubramanian, A. Bernamonti, B. Craps, V. Keränen, E. Keski-Vakkuri, B. Müller, L. Thorlacius, and J. Vanhoof, Thermalization of the spectral function in strongly coupled two dimensional conformal field theories, J. High Energy Phys. 04 (2013) 069.
- [31] N. Čeplak, H. Liu, A. Parnachev, and S. Valach, *Black hole singularity from OPE*, J. High Energy Phys. 10 (2024) 105.
- [32] M. Headrick, Entanglement Renyi entropies in holographic theories, Phys. Rev. D 82, 126010 (2010).
- [33] F. M. Haehl, T. Hartman, D. Marolf, H. Maxfield, and M. Rangamani, *Topological aspects of generalized gravitational entropy*, J. High Energy Phys. 05 (2015) 023.
- [34] L. Susskind and E. Witten, *The holographic bound in anti-de Sitter space*, arXiv:hep-th/9805114.
- [35] Y. Kusuki, T. Takayanagi, and K. Umemoto, *Holographic entanglement entropy on generic time slices*, J. High Energy Phys. 06 (2017) 021.
- [36] B. Liu, H. Chen, and B. Lian, Entanglement entropy of free fermions in timelike slices, Phys. Rev. B 110, 144306 (2024).
- [37] J. Erdmenger and N. Miekley, Non-local observables at finite temperature in AdS/CFT, J. High Energy Phys. 03 (2018) 034.
- [38] T. Hartman and J. Maldacena, Time evolution of entanglement entropy from black hole interiors, J. High Energy Phys. 05 (2013) 014.
- [39] M. Banados, C. Teitelboim, and J. Zanelli, *The black hole in three-dimensional space-time*, Phys. Rev. Lett. 69, 1849 (1992).
- [40] V. Balasubramanian, B. D. Chowdhury, B. Czech, and J. de Boer, *Entwinement and the emergence of spacetime*, J. High Energy Phys. 01 (2015) 048.

- [41] V. E. Hubeny, M. Rangamani, and E. Tonni, Global properties of causal wedges in asymptotically AdS spacetimes, J. High Energy Phys. 10 (2013) 059.
- [42] V.E. Hubeny, H. Liu, and M. Rangamani, *Bulk-cone singularities & signatures of horizon formation in AdS/CFT*, J. High Energy Phys. 01 (2007) 009.
- [43] M. Gary, S. B. Giddings, and J. Penedones, *Local bulk S-matrix elements and CFT singularities*, Phys. Rev. D **80**, 085005 (2009).
- [44] J. Maldacena, D. Simmons-Duffin, and A. Zhiboedov, Looking for a bulk point, J. High Energy Phys. 01 (2017) 013.
- [45] M. Dodelson, C. Iossa, R. Karlsson, A. Lupsasca, and A. Zhiboedov, *Black hole bulk-cone singularities*, J. High Energy Phys. 07 (2024) 046.
- [46] B. Czech, L. Lamprou, S. McCandlish, and J. Sully, *Integral geometry and holography*, J. High Energy Phys. 10 (2015) 175.
- [47] J. de Boer, M. P. Heller, R. C. Myers, and Y. Neiman, *Holographic de Sitter geometry from entanglement in conformal field theory*, Phys. Rev. Lett. **116**, 061602 (2016).
- [48] B. Czech, L. Lamprou, S. McCandlish, B. Mosk, and J. Sully, A stereoscopic look into the bulk, J. High Energy Phys. 07 (2016) 129.
- [49] J. de Boer, F. M. Haehl, M. P. Heller, and R. C. Myers, Entanglement, holography and causal diamonds, J. High Energy Phys. 08 (2016) 162.
- [50] A. Milekhin, Z. Adamska, and J. Preskill, Observable and computable entanglement in time, arXiv:2502.12240.
- [51] C. Nunez and D. Roychowdhury, Interpolating between space-like and time-like entanglement via holography, arXiv:2507.17805.